



## Wave-to-grid (W2G) control of a wave energy converter

Hafiz Ahsan Said<sup>a,\*</sup>, Demián García-Violini<sup>b</sup>, John V. Ringwood<sup>a</sup>

<sup>a</sup> Centre for Ocean Energy Research (COER), Department of Electronic Engineering, Maynooth University, W23 F2H6 Co. Kildare, Ireland

<sup>b</sup> Departamento de Ciencia y Tecnología, Universidad Nacional de Quilmes, R. S. Peña 352, Bernal B1876, Argentina

### ARTICLE INFO

#### Keywords:

Grid integration  
LiTe-Con  
Lyapunov control  
Wave-to-grid control

### ABSTRACT

Grid integration of wave energy involves various power train stages from device to grid, such as a power take-off stage, a power conversion stage, and a power conditioning stage. The coupled performance of the complete wave-to-grid system depends heavily on the dynamics of each stage and their respective controllers. However, the control objectives of various stages may not align with each other and pose a potential problem, in terms of economic performance and grid integration. This study presents a complete wave-to-grid control approach for a wave energy converter, ensuring that the system performs optimally under variable wave resource conditions. The proposed system comprises a point absorber wave energy converter oscillating in heave, a linear permanent magnet generator, and back-to-back power converters for connection to the grid. Additionally, short term energy storage, based on an ultra-capacitor, is also added to the DC link between the back-to-back converters for power quality improvement. In the paper, a mathematical model is derived for the individual components of the wave-to-grid system. Then, the controllers for each stage of the power train are designed. A LiTe-Con controller is used for maximum power extraction on the device side, while Lyapunov-based nonlinear controllers are designed for power converter control in order to achieve the full range of control objectives. The result shows that the proposed controllers accomplish the desired control objectives and perform well under various operating conditions.

### 1. Introduction

The excessive use of traditional fossil fuel power plants creates significant concerns for the modern world. These sources emit greenhouse gases in abundance, which is a primary cause of anthropogenic climate change. Renewable energy integration is vital in overcoming the perils of fossil fuel plants, with countries shifting towards renewable energy sources to meet their energy demands and to address the problems of climate change. Thus, to mitigate energy demand issues, wave energy has gained more attention during the past two decades, which has led to the development of various wave energy systems [1]. Wave energy will be instrumental in the transition towards a 100% renewable future due to the following reasons:

- The vast potential for clean energy. The worldwide theoretical wave energy potential is estimated at 16,000 TWh/year [2,3], which can be a considerable contribution towards meeting the increasing world's energy demands.
- The temporal complementarity of wave resource with other renewable resources, such as wind and solar, can lead to positive synergies

among these resources [4–6]. These synergies will enable the supply systems to accept renewable energy at lower costs than the existing system, which relies heavily on wind and solar power.

Like other renewable energy resources (RES), the wave energy resource is intermittent, relatively unpredictable and highly variable, posing a significant challenge for grid integration. There are various problems associated with wave energy grid integration, such as power output variability, control of power converters, and optimal storage requirements. Another layer of difficulty in wave energy is reactive wave energy converter (WEC) control implementation, which requires bidirectional power flow between the device and the grid. It is necessary to tackle the above mentioned problems to increase wave energy penetration into power grids.

The literature review presented in the paper focuses on complete wave-to-grid (W2G) modelling and control, which is a little different from a wave-to-wire (W2W) system. A W2W system includes WEC, PTO mechanism and generator-side converter. On the other hand, a W2G system not only includes WEC, PTO mechanism and generator-side converter; it also includes DC bus dynamics, storage converter, grid-

\* Corresponding author.

E-mail addresses: [hafiz.said.2020@mumail.ie](mailto:hafiz.said.2020@mumail.ie) (H.A. Said), [ddgv83@gmail.com](mailto:ddgv83@gmail.com) (D. García-Violini), [john.ringwood@mu.ie](mailto:john.ringwood@mu.ie) (J.V. Ringwood).

side converter and grid. Grid integration studies involving wave energy generally have some drawbacks, such as simplified hydrodynamic models, simplified power converter models and relatively rudimentary proportional integral (PI) power converter control [7]. For example, in [8–20], oversimplified hydrodynamic models are used; in particular the effects of radiation forces are not modelled correctly. Moreover, the simulation of monochromatic wave excitation is common for most grid integration studies [8,9,12,14–18], which does not represent real sea waves. Additionally, recent studies in the literature also suggests that the use of passive damping, as a maximum power extraction control, is the default choice of hydrodynamic control in terms of grid integration studies [8–12,14–18,21,22], which is very limited in extracting maximum power from the waves and fails to account for device constraints. Appropriate control of the associated power converters is also crucial for grid integration. Mostly, wave energy grid integration studies use PI control [8–12,14–18,21]. Linear PI controllers for power converters are not always the best control mechanism in all operating ranges because of the nonlinear nature of power converter models [22]. As a result, tuning PI controllers to ensure stability over the entire operational envelope can be challenging. However, in some cases, PI controllers are tuned optimally by using various algorithms such as a water cycle algorithm in [15], and a multi-objective salp swarm algorithm in [20]. Still, the oversimplification of the WEC models limits the validity of these studies. Multiple papers in the W2W literature provide modelling and reactive hydrodynamic control on the device side [23–34] but few studies provide sufficient information for the DC bus and grid-side. W2W models differ for different WECs and PTO mechanisms. For example, a W2W model of an oscillating water column (OWC) is presented in [26], and [31] presents a high fidelity W2W model for a point absorber WEC. A detailed review of various W2W models is presented in [27]. In [32], a passivity based piece-wise velocity control method is designed for a direct drive W2W system while, in [25,28], the authors added the effects of copper losses and field weakening in a model predictive control (MPC) formulation to extract maximum power from waves. However, little attention is given to the power converter models and grid-side control. In [34], the authors simulated both passive and reactive hydrodynamic controllers for a W2W system though, for a grid-connected case study, only a passive hydrodynamic controller is implemented. As far as grid integration is concerned, our current paper provides a mechanism for reactive hydrodynamic control implementation for W2G operation of a grid-connected WEC.

In addition, the important role of energy storage for wave energy grid integration cannot be overstated. Energy storage systems allow excess power storage and improve the power quality of the intermittent and unpredictable wave resource. Energy storage also provides negative power for reactive control implementation on the device side. A review of energy storage technologies for marine applications is presented in [35]. Short term storage, such as systems based on ultra-capacitors (UCs) [36], and high-speed kinetic buffers [37], are gaining popularity for wave energy applications, due to their fast response times. In addition, a hybrid energy storage system (HESS), which benefits from two or more storage systems, is also used for wave energy applications [38–40].

This paper presents a complete wave-to-grid (W2G) control approach for a direct drive heaving point absorber WEC, including balanced, high-performance, control of both device and grid sides. Here, hydrodynamic control of the WEC is based upon the (Linear Time invariant Controller) LiTe-Con [41], which aims to maximise power extraction from the waves and provides a constraint handling mechanism. At the same time, nonlinear Lyapunov control is proposed for the power converters. The contribution of the paper can be summarised as follows:

- A complete balanced-fidelity control-oriented W2G model for a direct drive WEC is presented.
- High-performance controllers for both device-side (LiTe-Con) and grid side (Lyapunov control) are proposed.

- A UC-based storage system is included for power quality improvement and reactive hydrodynamic control support.
- An energy management system as a supervisory control mechanism is also proposed, which ensures proper operation of storage converter for DC bus voltage regulation and reactive LiTe-Con control support.

The proposed W2G system is shown in Fig. 1, consisting of three subsystems, i.e.:

1. A device-side subsystem (a WEC, a linear permanent magnet generator and AC/DC converter).
2. A storage subsystem, comprising an ultra-capacitor and a DC/DC buck-boost converter.
3. A grid-side subsystem that includes a DC/AC inverter and a grid model.

The WEC and linear permanent magnet generator (LPMG) are connected to the DC bus through an active rectifier, referred to as a generator-side converter (Gen-SC). In addition, the UC is connected to the DC bus via a bidirectional buck-boost converter. A DC/AC inverter, referred to as a grid-side converter (Grid-SC), connects the DC link to the grid. Gen-SC control focuses on hydrodynamic control, responsible for maximum power extraction from the waves. In contrast, the DC/DC converter control objective, for the storage system, revolves around power quality improvement through DC bus voltage regulation and the provision of support for hydrodynamic control. Finally, maximum active power is injected into the grid via the Grid-SC.

Gen-SC and Grid-SC combine to form a fully-rated back-to-back (b2b) power converter configuration for a grid-connected WEC. The choice of fully-rated power converters is motivated by the following requirements/benefits. Firstly, the full-speed range control of a LPMG requires a fully-rated power converter (FPC) configuration. Secondly, The bi-directional power flow requirement of the reactive hydrodynamic control also requires an active full-rated converter. Finally, the FPC configuration provides a natural disconnection in the form of a DC-link that effectively decouples Gen-SC and Grid-SC control.

The remainder of the paper is organised as follows: Section 2 describes the modelling of various components of the W2G system, while Section 3 discusses the considered W2G control approach, which covers the control of both the WEC and the power converters, based on LiTe-Con and Lyapunov control, respectively. Grid synchronisation through a phase-locked loop (PLL) is discussed in Section 4, while Section 5 presents the results of the study. Conclusions on the overall control design procedure are provided in Section 6.

## 2. Modelling of the W2G system

As described in Section 1, the complete W2G system contains three subsystems, i.e., device-side, Grid-side, and storage subsystem. A detailed schematic of the W2G system is shown in Fig. 3.

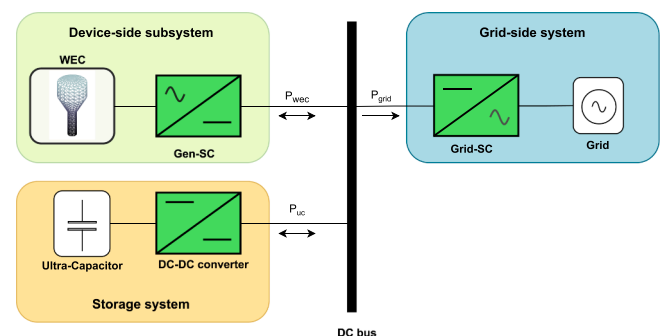


Fig. 1. Proposed W2G system.

## 2.1. Modelling of wave energy conversion system [Device-side subsystem]

The wave energy system comprises a WEC, LPMG and Gen-SC. The modelling of each component is described in the following subsections.

### 2.1.1. WEC model

A single body floating WEC, oscillating in heave, is considered in this study. The LPMG translator is rigidly connected to the WEC. The WEC heave motion drives the translator of the LPMG. The WEC, the PTO system, and the forces acting on the system are shown in Fig. 2.

The dynamics of the WEC in the time domain can be represented by:

$$\mathcal{M}\ddot{z}(t) = f_{exc}(t) + f_r(t) + f_{hs}(t) - f_{pto}(t), \quad (1)$$

where,  $f_{exc}(t)$  is the uncontrollable excitation force due to the incoming wave field,  $f_r(t)$  is the radiation force and  $f_{hs}(t)$  is the linearised hydrostatic force.  $f_{pto}(t)$  represents the control force applied by the LPMG on the WEC.  $\mathcal{M}$  is the total mass of the oscillating system, while  $z(t), \dot{z}(t) = v(t)$ , and  $\ddot{z}(t)$  represent heave displacement, velocity and acceleration, respectively. The hydrostatic stiffness force is given by<sup>1</sup>:

$$f_{hs} = -K_{hs}z, \quad (2)$$

where  $K_{hs} > 0$  is the hydrostatic stiffness coefficient. The radiation force  $f_r$ , which represents the fluid force induced by the body motion in generating waves, is modelled through linear potential flow theory, using Cummins' equation [42], as follows:

$$f_r = -m_{\infty}\ddot{z} - k_r^* \dot{z}, \quad (3)$$

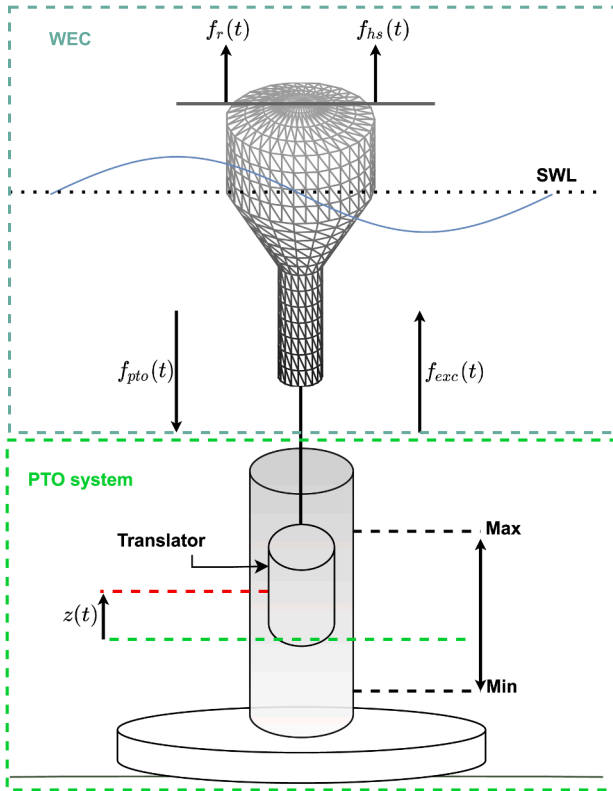


Fig. 2. WEC and PTO (LPMG) system considered in this study. The acronym SWL stands for still water level.

where  $m_{\infty} = \lim_{\omega \rightarrow +\infty} A(\omega)$ , with  $A(\omega)$  termed the radiation added mass, is the added mass at infinite frequency, and  $k_r$  is the (causal) radiation impulse response function. The operator  $*$  represents the convolution operator. Finally, the equation of motion, from (1), is given by:

$$(\mathcal{M} + m_{\infty})\ddot{z} + k_r^* \dot{z} + K_{hs}z = f_{exc} - f_{pto}. \quad (4)$$

Note that, as generally considered in the WEC field [43], the radiation convolution term,  $k_r^* \dot{z}$ , can be approximated using a linear time invariant (LTI) state-space representation, as Eq. (5), where  $A_r, B_r, C_r$ , and  $D_r$ , can be obtained using standard system identification toolboxes as, for example, the FOAMM toolbox [44].

$$\begin{aligned} \dot{Y}_r &= A_r Y_r + B_r \dot{z} \\ f_{rc} &= C_r Y_r \approx k_r^* \dot{z} \end{aligned} \quad (5)$$

Since the LTI hydrodynamic control, considered in Section 3, is frequency-domain based, the frequency domain mapping  $G_{wec}(j\omega)$  characterising the WEC dynamics is calculated as:

$$G_{wec}(j\omega) = \frac{j\omega}{K_{hs} - \omega^2(\mathcal{M} + m_{\infty}) + j\omega K_r(j\omega)} \quad (6)$$

with

$$V(j\omega) = G_{wec}(j\omega) [F_{exc}(j\omega) - F_{pto}(j\omega)] \quad (7)$$

### 2.1.2. LPMG and AC/DC (Gen-SC) converter model

High force density and reasonable efficiency, at low speeds, give rise to the use of a LPMG as a power-take-off (PTO) mechanism for direct-drive wave energy applications [45]. The dynamic model of the LPMG is very similar to a rotary permanent magnet generator. The only difference is the motion of the translator, which reciprocates as compared to the rotating rotor for a rotary generator. Utilising the  $d$ - $q$  (Park) transformation [46], a two-phase system can represent a balanced three-phase system [47], where the transformation matrix relies on the electrical angular position  $\theta(t)$ . In the case of a LPMG, the angular position depends on the heave displacement of the translator:

$$\theta(t) = \frac{\pi}{\tau} z(t). \quad (8)$$

Assuming the LPMG is symmetric, the dynamic model of the LPMG in the  $d$ - $q$  frame, given in [48], is:

$$\frac{d\lambda_d}{dt} = -v_{ds} - i_{ds}R_s + \lambda_q\omega_e \quad (9)$$

$$\frac{d\lambda_q}{dt} = -v_{qs} - i_{qs}R_s + \lambda_d\omega_e \quad (10)$$

with,

$$\lambda_d = L_d i_{ds} - \psi_{PM} \text{ and } \lambda_q = L_q i_{qs} \quad (11)$$

where,  $v_{ds,qs}, i_{ds,qs}$  and  $L_{d,q}$  are the  $d$ - and  $q$ -axis stator voltages, currents, and inductances, respectively,  $\psi_{PM}$  is the permanent magnet flux linkage, and  $R_s$  is the stator resistance. In addition,  $\omega_e$ , in Eq (9) and (10), is the angular frequency of the stator variables, calculated as:

$$\omega_e = \frac{\pi}{\tau} \dot{z}, \quad (12)$$

where  $\tau$  is the pole pitch of the LPMG. The PTO force, produced by the LPMG, depends on the stator currents, the flux linkage, and the pole pitch, as shown below:

$$f_{pto}(t) = 1.5 \frac{\pi}{\tau} (\lambda_d i_{qs} - \lambda_q i_{ds}) \quad (13)$$

Using the flux relations, given in the Eq. (11),  $f_{pto}(t)$  can be calculated as:

<sup>1</sup> From now on, the dependence on  $t$  is dropped when clear from the context.

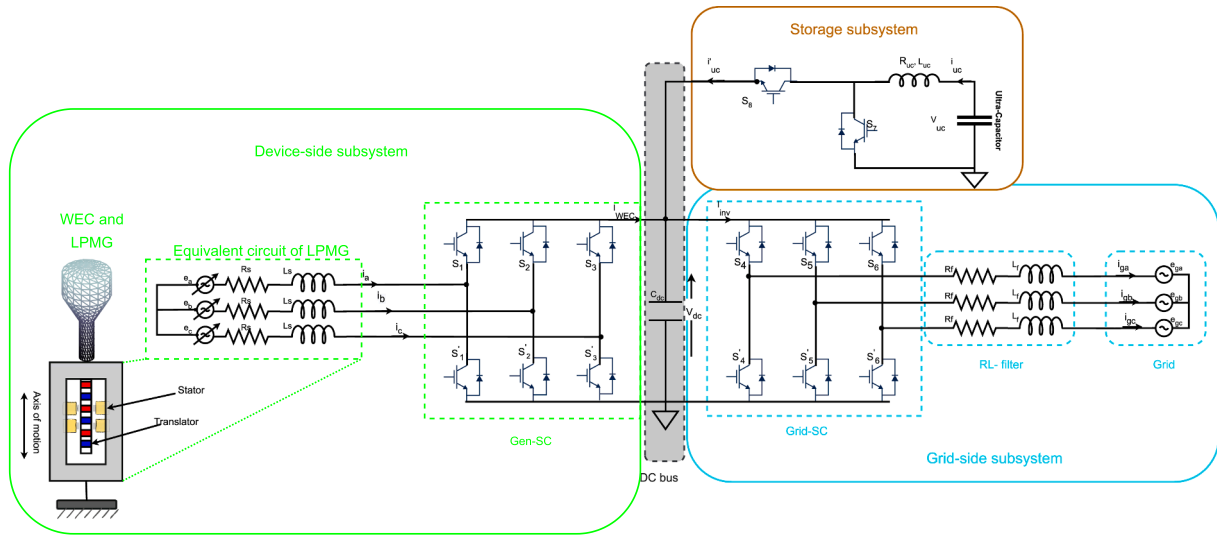


Fig. 3. A complete schematic of the W2G system.

$$f_{plo}(t) = 1.5 \frac{\pi}{\tau} \left( (L_d - L_q) i_{ds} i_{qs} - \psi_{PM} i_{qs} \right) \quad (14)$$

Eq. (14) implies that the developed force of an LPMG consists of two components. The first term represents the reluctance force due to saliency, while the second term is the magnetic force produced by the permanent magnet. For simplicity, a surface mount (non-salient) LPMG machine is considered here;  $d$ - and  $q$ -axis inductances are therefore equal i.e.  $L_d = L_q = L_s$ . Using  $L_d = L_q = L_s$ , the model, from (9), (10) and (14), can be expressed as:

$$\frac{di_{ds}}{dt} = -\frac{R_s}{L_s} i_{ds} + \omega_e i_{qs} - \frac{1}{L_s} v_{ds}, \quad (15)$$

$$\frac{di_{qs}}{dt} = -\omega_e i_{ds} - \frac{R_s}{L_s} i_{qs} - \frac{\omega_e}{L_s} \psi_{PM} - \frac{1}{L_s} v_{qs}, \quad (16)$$

with,

$$f_{plo} = -1.5 \frac{\pi}{\tau} \psi_{PM} i_{qs}. \quad (17)$$

Since the stator  $d$ - and  $q$ -axis voltages act as the inputs to the Gen-SC and can be controlled independently, these voltages are now expressed in terms of corresponding converter control actions [49,50], as follows:

$$v_{ds} = v_{dc} u_{ds}, \quad v_{qs} = v_{dc} u_{qs}, \quad \text{and} \quad i_{wec} = u_{ds} i_{ds} + u_{qs} i_{qs} \quad (18)$$

where  $u_{ds}$  and  $u_{qs}$  are the Park transformation of the triphase duty ratio system, i.e.,  $S_i, \forall i = 1, 2, 3$ , see Fig. 3, with

$$S_i = \begin{cases} 1 & \text{if } S_i \text{ is ON and } S'_i \text{ is OFF} \\ 0 & \text{if } S_i \text{ is OFF and } S'_i \text{ is ON} \end{cases} \quad (19)$$

Substituting the values of  $v_{ds}$  and  $v_{qs}$  from Eq. (18) into Eqs. (15) and (16), the unified model, of the generator-rectifier combination, is obtained as follows:

$$\frac{di_{ds}}{dt} = -\frac{R_s}{L_s} i_{ds} + \omega_e i_{qs} - \frac{1}{L_s} v_{dc} u_{ds} \quad (20)$$

$$\frac{di_{qs}}{dt} = -\omega_e i_{ds} - \frac{R_s}{L_s} i_{qs} - \frac{\omega_e}{L_s} \psi_{PM} - \frac{1}{L_s} v_{dc} u_{qs} \quad (21)$$

## 2.2. DC/AC inverter (Grid- SC) modelling [Grid-side subsystem]

The DC/AC inverter (Grid-SC) is shown on right-hand side of Fig. 3.

Similar to the Gen-SC, it is a three-legged, three phase converter with six IGBTs. The dynamic model of the Grid-SC can be obtained [51,49], using Kirchoff's laws, as follows:

$$L_f \frac{di_{g(abc)}}{dt} = v_{dc} [S_j] - v_{g(abc)} - R_f i_{g(abc)} \quad (22)$$

where,  $i_{g(abc)} = [i_{ga}, i_{gb}, i_{gc}]^T$  are the three phase grid currents,  $v_{g(abc)} = [v_{ga}, v_{gb}, v_{gc}]^T$  are the sinusoidal three phase grid voltages,  $R_f$  is the filter resistance, and  $L_f$  is the filter inductance. In addition, in Eq. (22),  $S_j, \forall j = 4, 5, 6$ , is the switch position function, defined as follows:

$$S_j = \begin{cases} 1 & \text{if } S_j \text{ is ON and } S'_j \text{ is OFF} \\ 0 & \text{if } S_j \text{ is OFF and } S'_j \text{ is ON} \end{cases} \quad (23)$$

For control synthesis, the triphase representation, in Eq. (23), is simplified by using  $d$ - $q$  transformation. The  $d$ - $q$  frame is linked with the grid voltage and rotates synchronously with grid voltage frequency  $\omega_o$ , which results in the following model for the DC/AC inverter [49].

$$\frac{di_{dg}}{dt} = -\frac{V_{dg}}{L_f} + \omega_o i_{qg} - \frac{R_f}{L_f} i_{dg} + \frac{v_{dc}}{L_f} u_{dg}, \quad (24)$$

$$\frac{di_{qg}}{dt} = -\omega_o i_{dg} - \frac{R_f}{L_f} i_{qg} + \frac{v_{dc}}{L_f} u_{qg}, \quad (25)$$

where,  $i_{dg,qg}$  denotes grid currents in the  $d$ - $q$  frame and  $u_{dg,qg}$  are the  $d$ - $q$  components of the triphase duty ratio system  $S_j$ .

## 2.3. Ultra-capacitor and buck-boost converter model [Storage subsystem]

The use of a UC-based storage system for the W2G controlled operation is essential for the following reasons. First, the WEC hydrodynamic control works on the basic principle of exaggerating the device motion in resonance with the wave resource. The variability in the WEC output power is increased under controlled WEC conditions due to the exaggerated movement of the device. The highly variable WEC output power cannot be directly fed into the grid due to the power quality requirements imposed by the grid codes. Hence, using the UC storage decreases the variability in the WEC electrical output power, increasing the value of the grid-connected wave power. Secondly, an essential factor is the reactive LiTe-Con control implementation on the device side. LiTe-Con is based upon the principle of the complex conjugate control of WEC, which requires power from the grid-side at some

instances for proper operation, which cannot be supported with only Grid-SC control, but requires the additional storage system controller. Therefore, the negative (reactive) power requirements of LiTe-Con, in addition to DC bus voltage regulation, is met by the UC storage system. In this way, the UC storage system allows for, and requires, decoupled controllers on either side of the DC bus.

The buck-boost converter operates in both boost and buck mode, depending upon the direction of power flow. The UC supplies power to the DC link in discharge mode, and the converter works as a boost converter ( $S_7$  ON,  $S_8$  OFF). On the other hand, the DC/DC converter operates in buck mode during charge mode ( $S_7$  OFF,  $S_8$  ON) and power from the DC bus charges the UC. During discharge mode, the model is easily derived [51,52] as:

$$\frac{di_{uc}}{dt} = \frac{V_{uc}}{L_{uc}} - \frac{R_{uc}}{L_{uc}}i_{uc} - (1 - u_7)\frac{v_{dc}}{L_{uc}}, \quad (26)$$

$$\dot{i}_{uc} = (1 - u_7)i_{uc}, \quad (27)$$

while, during charge mode, the model is derived as follows:

$$\frac{di_{uc}}{dt} = \frac{V_{uc}}{L_{uc}} - \frac{R_{uc}}{L_{uc}}i_{uc} - u_8\frac{v_{dc}}{L_{uc}}, \quad (28)$$

$$\dot{i}_{uc} = u_8i_{uc}, \quad (29)$$

where,  $V_{uc}$ ,  $L_{uc}$ , and  $R_{uc}$  are UC voltage, inductance and equivalent series resistance, respectively,  $i_{uc}$  and  $\dot{i}_{uc}$  are the UC input and output currents.  $u_7$  and  $u_8$  are the control signals for switches  $S_7$  and  $S_8$ . For simplicity, a signal  $u_{78}$  is introduced as:

$$u_{78} = K(1 - u_7) + (1 - K)u_8, \quad (30)$$

with  $K$  defined as:

$$K = \begin{cases} 1 & \text{if } S_7 \text{ is ON and } S_8 \text{ is OFF (Boost mode)} \\ 0 & \text{if } S_7 \text{ is OFF and } S_8 \text{ is ON (Buck mode)} \end{cases}.$$

Finally, the simplified model for the DC/DC converter, using  $u_{78}$ , gives:

$$\frac{di_{uc}}{dt} = \frac{V_{uc}}{L_{uc}} - \frac{R_{uc}}{L_{uc}}i_{uc} - \frac{v_{dc}}{L_{uc}}u_{78}, \quad (31)$$

$$\dot{i}_{uc} = u_{78}i_{uc}. \quad (32)$$

#### 2.4. Complete power conversion system model

The mathematical models obtained in Sections 2.1.2, 2.2, and 2.3, for LPMG and Gen-SC combination, Grid-SC, and buck-boost converter, respectively, are put together to form complete power conversion system model. From Fig. 3, it follows that:

$$C_{dc}\frac{dv_{dc}}{dt} = i_{wec} + \dot{i}_{uc} - i_{inv}, \quad (33)$$

and, using Eqs. (18) and (32) in Eq. (33), gives:

$$\frac{dv_{dc}}{dt} = \frac{1}{C_{dc}} \left[ \left( u_{ds}i_d + u_{qs}i_q \right) + u_{78}i_{uc} - i_{inv} \right]. \quad (34)$$

For control design, it is convenient to use averaged models<sup>2</sup> for the power converters, based on replacing all the variables of the model by their respective average values over a switching period [54,55]. This modelling technique determines the state model for each possible circuit configuration and then combines all these elementary models into a unified one through a duty ratio. The averaged models are useful for

control applications due to their simplicity and fast computational times [53]. In this regard, we define averaged state variables as  $x_1 = \langle i_{ds} \rangle$ ,  $x_2 = \langle i_{qs} \rangle$ ,  $x_3 = \langle i_{dg} \rangle$ ,  $x_4 = \langle i_{qg} \rangle$ ,  $x_5 = \langle i_{uc} \rangle$  and  $x_6 = \langle v_{dc} \rangle$ , where the operator  $\langle \bullet \rangle$  represent the average value over a switching period. Combining Eqs. (20), (21), (24), (25), (32) and (34) results in the following complete power conversion system model.

$$\frac{dx_1}{dt} = -\frac{R_s}{L_s}x_1 + \omega_e x_2 - \frac{x_6}{L_s}\mu_{ds} \quad (35)$$

$$\frac{dx_2}{dt} = -\omega_e x_1 - \frac{R_s}{L_s}x_2 - \frac{\omega_e}{L_s}\psi_{PM} - \frac{x_6}{L_s}\mu_{qs} \quad (36)$$

$$\frac{dx_3}{dt} = -\frac{V_{dg}}{L_f} + \omega_o x_4 - \frac{R_f}{L_f}x_3 + \frac{x_6}{L_f}\mu_{dg} \quad (37)$$

$$\frac{dx_4}{dt} = -\omega_o x_3 - \frac{R_f}{L_f}x_4 + \frac{x_6}{L_f}\mu_{qg} \quad (38)$$

$$\frac{dx_5}{dt} = \frac{V_{uc}}{L_{uc}} - \frac{R_{uc}}{L_{uc}}x_4 - \frac{x_6}{L_{uc}}\mu_{78} \quad (39)$$

$$\frac{dx_6}{dt} = \frac{1}{C_{dc}} \left[ \left( \mu_{ds}x_1 + \mu_{qs}x_2 \right) + \mu_{78}x_5 - i_{inv} \right] \quad (40)$$

where,  $\mu_{ds}$ ,  $\mu_{qs}$ ,  $\mu_{dg}$ ,  $\mu_{qg}$  and  $\mu_{78}$  are the duty ratios of the Gen-SC, Grid-SC and DC/DC storage converter.

### 3. W2G controller design

#### 3.1. Overall W2G control philosophy

A W2G system involves a variety of stages of the power train, including absorption, transmission and conditioning stages [7]. As mentioned earlier, in Section 1, the DC bus serves to decouple different subsystems in the power train. Each stage has its own specific requirements, which translated into control objectives, guides the overall W2G control philosophy. On the device side, for example, the requirements include maximum power extraction from waves, subject to WEC motion constraints and LPMG Copper (Cu) loss minimisation. On the other hand, the grid side requirements are imposed by the grid codes (e.g. [56]) which sets conditions on the quality of power (frequency, voltage, total harmonic distortion (THD) levels etc.), injected into the grid. The difficulty arises when the control objectives on either side of the DC bus do not align, i.e. maximum power extraction from waves leads to increased peak power on the DC bus due to device motion exaggeration, with potentially poor resulting power quality at the DC bus, which is contrary to the requirements of grid-side control. In addition, reactive hydrodynamic controllers, such as LiTe-Con, require reactive (negative) power from the DC bus. This power is needed to accelerate/decelerate the device to achieve the resonance condition required by controllers based on the complex conjugate principle, adding another layer of difficulty in implementation. The requirements and problems mentioned above are tackled using two specific elements in the power train: storage and W2G control.

Fig. 4 illustrates this interplay among the different subsystems in the power train. Fully-rated back-to-back converters, with a DC link and UC storage, are used to minimise the interaction among different controllers. Back-to-back converter control and UC storage provide a decoupled control mechanism on either side of the DC link. Additionally, an energy management system (EMS), as a supervisory control mechanism, is added to the DC bus, ensuring the proper operation of the low-level storage controller required for decoupled operation on both sides of the DC bus. The use of storage allows the isolation of the controllers on both sides by DC bus voltage regulation and the support of hydrodynamic control. In this regard, storage sizing is important, because it has to perform two tasks. Firstly, DC bus voltage regulation must be

<sup>2</sup> The interested reader is referred to [53–55] for comprehensive description of averaging methods for power converter models.



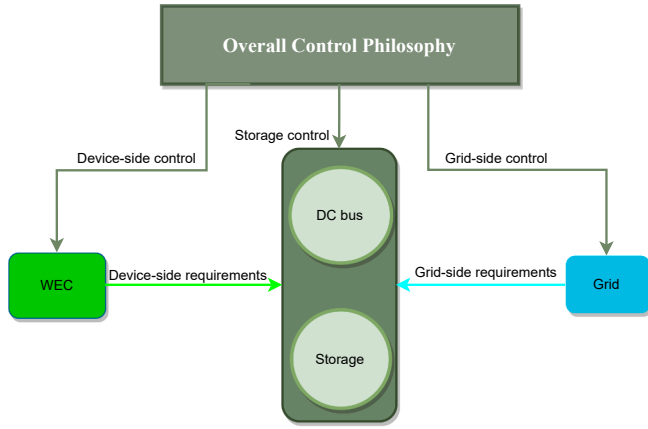


Fig. 4. W2G control philosophy.

achieved, by absorbing power peaks at the DC bus. Secondly, storage provides support for reactive hydrodynamic control (LiTe-Con), by feeding negative electrical power back to the LPMG, when required. In this way, the interaction among various controllers for W2G controlled operation is minimised. The storage control and energy management strategy is discussed in detail in Section 3.4.

The selection of storage size is based upon the method presented in [13], where a worst-case scenario is assumed. It is assumed that inverter provides constant power to the grid at the highest wave energy period ( $T_p = 12$  s). The constant power is based on the mean power calculated at the DC bus when WEC is operated under LiTe-Con control, which results in 8.65kW power. A storage capacity of about ten times the wave period will provide constant output power to the grid in most wave conditions, as stated in [57]. Hence, allowing UC storage to store ten times the output WEC power will lead to a storage capacity of 1.20kWh, with a rate of change of power of 50 s. The rate of change of power is based upon the time constant of the low-pass filter used in the energy management system (EMS), as explained in Section 3.4. The UC storage helps in power smoothing and DC bus voltage regulation by removing WEC electrical output power peaks. The parameters of the UC storage system are presented in Table A1.

The control objectives of the W2G control approach are summarised as:

1. Maximum power extraction from the waves by tracking a reference PTO force generated through hydrodynamic (LiTe-Con/passive damping) control.
2. Generator Cu-losses minimisation by regulating LPMG stator  $q$ -axis current  $i_{qs}$  to zero.
3. Maximum active power injection into the grid by tracking  $i_{dg}$  to its reference.
4. Unity power factor control by regulating  $i_{qg}$  to zero.
5. DC bus voltage regulation and the support for reactive hydrodynamic control by tracking UC current  $i_{uc}$  to its reference.

### 3.2. Control of the device side subsystem

#### 3.2.1. LiTe-Con hydrodynamic control (reference generation for Gen-SC control)

The LiTe-Con energy maximising controller, proposed in [41], in essence, aims to approximate the optimal frequency-domain condition for absorbed-energy maximisation, given by the impedance-matching

(or complex-conjugate) principle. In general, as shown in [41,58], this control approach provides a high-performance control solution while being suitable for realistic scenarios, due to its broadband nature and the inclusion of a constraint handling mechanism, respectively. In particular, LiTe-Con is computationally efficient, compared to optimisation based controllers [59]. Among simple WEC controllers, i.e. based on the impedance-matching principle without the inclusion of optimisation routines, LiTe-Con provides the best performance in terms of maximum power capture and constraint handling, as shown in [60]. It is worth highlighting that, given the feedforward nature of LiTe-Con, this controller can effectively deal with well-known limitations in feedback impedance-matching-based controllers, such as stability or constraint handling. In particular, in contrast with similar controllers in the literature based on the impedance-matching principle, the LiTe-Con has the added capability of handling motion constraints [60], which makes this controller appealing for realistic WEC control implementations, where WEC motion is significantly exaggerated. Furthermore, application of the LiTe-Con has been validated in a realistic and experimental environment in [58]. LiTe-Con is a reactive controller, meaning that it requires ‘reactive power’ from the DC-link at some instances for its proper operation. It is worth mentioning that this ‘reactive power’ is not the same as electrical reactive power, so a distinction should be made when talking about reactive power in the hydrodynamic control sense, by comparison with the electrical side. Fig. 5 illustrates the concept of electrical power flow conventions, for both active power  $P$  and reactive power  $Q$ , in bi-directional power flow applications. In hydrodynamic control of WEC, the required reactive power from the DC link is, in fact, the negative (active) electrical power, which lies in the second and third quadrant, as illustrated by the shaded region in the Fig. 5. From now on, the reactive power in hydrodynamic sense is referred to as the ‘mechanical reactive power’, while the reactive power in electrical sense is referred to as the ‘electrical reactive power’.

In order to obtain an analytical derivation of the LiTe-Con, the WEC force-to-velocity mapping, given in (6), can be expressed as:

$$G_{wec}(s)|_{s=j\omega} = \text{Re}\{G_{wec}(\mathcal{J}\omega)\} + \mathcal{J}\text{Im}\{G_{wec}(\mathcal{J}\omega)\}, \quad (41)$$

where  $\text{Re}$  and  $\text{Im}$  denote the real-part and imaginary-part operators, respectively, while  $G_{wec}(s)$  is the WEC system representation in its transfer-function form. For the sake of simplicity of notation, let  $\text{Re}(G_{wec}) = \text{Re}\{G_{wec}(\mathcal{J}\omega)\}$  and  $\text{Im}(G_{wec}) = \text{Im}\{G_{wec}(\mathcal{J}\omega)\}$ . Then, using the expression in Eq. (41), the optimal force-to-velocity mapping, i.e. from  $f_{ex}(t)$  to  $v(t)$ , can be expressed as:

$$T_{f_{ex} \rightarrow v}^{opt}(\omega) = \frac{\text{Re}(G_{wec})^2 + \text{Im}(G_{wec})^2}{2\text{Re}(G_{wec})}. \quad (42)$$

Using the definitions in Eqs. (41) and (42), the optimal feedforward controller, that achieves the impedance-matching condition, can be expressed as:

$$K_{ff}^{opt}(\omega) = \frac{\text{Re}(G_{wec}) + \mathcal{J}\text{Im}(G_{wec})}{2\text{Re}(G_{wec})}. \quad (43)$$

Then, using system identification algorithms [61,62,43], the LiTe-Con aims to approximate the frequency-domain mapping  $K_{ff}^{opt}(\mathcal{J}\omega)$  with a parametric LTI-stable and implementable dynamical system  $K_{ff}^{LC}(s)$ , i.e.:

$$K_{ff}^{LC}(s)|_{s=j\omega} \approx K_{ff}^{opt}(\omega). \quad (44)$$

The control structure, required for the implementation of the LiTe-Con,

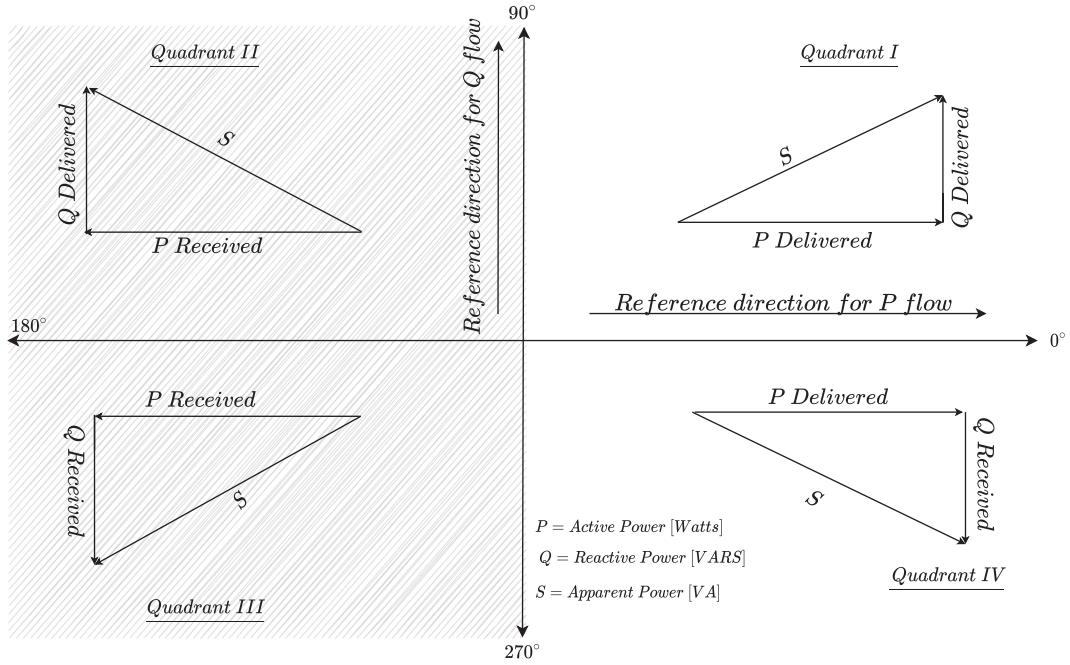


Fig. 5. Four quadrant electrical power flow naming convention in bi-directional power flow applications.

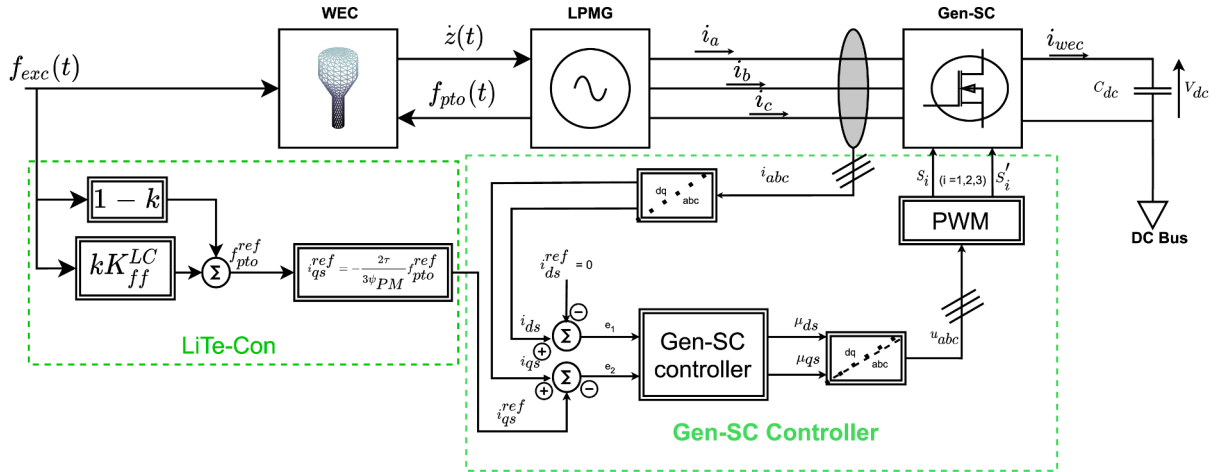


Fig. 6. Device-side control structure including LiTe-Con and Gen-SC control.

is schematically illustrated in Fig. 6. The interested reader is referred to [41] for a comprehensive discussion on the derivation, and practical considerations, of the LiTe-Con.

In order to implement the LiTe-Con controller in a realistic environment, a constraint handling mechanism is essential to prevent inflicting damage on the mechanical system. In particular, [41] proposes a constraint handling mechanism, using a constant value  $k \in [0, 1]$ , so that the resulting control force reference  $f_{pto}^{ref}$  for Gen-SC control, can be expressed as:

$$f_{pto}^{ref} = \left[ kK_{ff}^{LC}(s) + (1 - k) \right] f_{exc}. \quad (45)$$

$f_{pto}^{ref}$ , from Eq. (45), is used to generate the reference current for Gen-SC control. It is evident, from Eq. (17), that the force generated by the LPMG can be controlled with only q-axis current  $i_{qs}$ . Therefore,  $i_{qs}^{ref}$  is generated by using Eqs. (17) and (45) as:

$$i_{qs}^{ref} = -\frac{2\tau}{3\psi_{PM}} f_{pto}^{ref} \quad (46)$$

### 3.2.2. Lyapunov control of Gen-SC

The choice of Lyapunov control or so-called ‘stabilising control’, for the Gen-SC, and other power converters in the complete W2G system, is motivated by the fact that the converters are intrinsically nonlinear, with Lyapunov control especially effective for non-linear systems. Among nonlinear controllers used for power converter control, Lyapunov-based stabilising control is computationally efficient and ensures the stability of the system using the Lyapunov stability criterion [63]. The theoretical development and the application of various Lyapunov-based techniques to a broad class of practical engineering systems, such as electric machines and robotic systems etc., are presented in [64]. Fig. 6 represents the device-side control structure, including the hydrodynamic LiTe-Con controller.

The LPMG  $d$ - and  $q$ -axis currents are controlled via the Gen-SC. In this regard,  $i_{ds}^{ref}$  is set to zero, to minimise generator Cu-losses, and  $i_{qs}^{ref}$  is generated through Eq. (46) for maximum power extraction. To this end, the following tracking error signals are introduced:

$$e_1 = x_1 - i_{ds}^{ref} \quad (47)$$

$$e_2 = x_2 - i_{qs}^{ref} \quad (48)$$

To achieve the control objectives 1 and 2, listed in Section 3.1,  $e_1$  and  $e_2$  must be regulated to zero. Using (35) and (36), the dynamics of  $e_1$  and  $e_2$  can be derived as:

$$\dot{e}_1 = -\frac{R_s}{L_s}x_1 + \omega_e x_2 - \frac{1}{L_s}x_6\mu_{ds} - i_{ds}^{ref} \quad (49)$$

$$\dot{e}_2 = -\omega_e x_1 - \frac{R_s}{L_s}x_2 - \frac{\omega_e}{L_s}\psi_{PM} - \frac{1}{L_s}x_6\mu_{qs} - i_{qs}^{ref} \quad (50)$$

To drive  $e_1$  and  $e_2$  to zero,  $\dot{e}_1$  and  $\dot{e}_2$  are forced to behave as:

$$\dot{e}_1 = -c_1 e_1 \quad (51)$$

$$\dot{e}_2 = -c_2 e_2 \quad (52)$$

where  $c_1 > 0$  and  $c_2 > 0$ , are design parameters. Then, the comparison of Eqs. (49) and (50) with Eqs. (51) and (52), respectively, results in the following control laws for the Gen-SC:

$$\mu_{ds} = \frac{1}{x_6} \left[ -R_s x_1 + \omega_e L_s x_2 + c_1 e_1 L_s - L_s i_{ds}^{ref} \right] \quad (53)$$

$$\mu_{qs} = \frac{1}{x_6} \left[ -\omega_e L_s x_1 - R_s x_2 - \omega_e \psi_{PM} + c_2 e_2 L_s - L_s i_{qs}^{ref} \right] \quad (54)$$

### 3.3. Control of Grid-SC

The Grid-SC control is responsible for maximum active power and

zero electrical reactive power (unity power factor) injection into the grid. This is achieved through current control of Grid-SC. A PLL, which is utilised for grid phase tracking, as detailed in Section 4, is used to synchronise Grid-SC and grid voltages. The reference  $d$ -axis current  $i_{dg}^{ref}$  is derived from the energy management strategy, presented in Section 3.4, and the  $q$ -axis reference  $i_{qg}^{ref}$  is set to zero for unity power factor control. The Grid-SC control structure is shown in Fig. 7.

The current tracking errors are defined as:

$$e_3 = x_3 - i_{dg}^{ref} \quad (55)$$

$$e_4 = x_4 - i_{qg}^{ref} \quad (56)$$

To achieve the control objectives 3 and 4 listed in Section 3.1,  $e_3$  and  $e_4$  must be regulated to zero. Using (37) and (38), the dynamics of  $e_3$  and  $e_4$  can be derived as:

$$\dot{e}_3 = -\omega_o x_3 - \frac{R_f}{L_f}x_4 + \frac{x_6}{L_f}\mu_{qg} - i_{dg}^{ref} \quad (57)$$

$$\dot{e}_4 = -\omega_o x_3 - \frac{R_f}{L_f}x_4 + \frac{x_6}{L_f}\mu_{qg} - i_{qg}^{ref} \quad (58)$$

To drive errors  $e_3$  and  $e_4$  asymptotically to zero,  $\dot{e}_3$  and  $\dot{e}_4$  are forced to behave as:

$$\dot{e}_3 = -c_3 e_3 \quad (59)$$

$$\dot{e}_4 = -c_4 e_4 \quad (60)$$

where,  $c_3 > 0$  and  $c_4 > 0$ , are further design parameters. Comparing Eqs. (57) and (58) to Eqs. (59) and (60) results in the following control laws for the Grid-SC:

$$\mu_{dg} = \frac{1}{x_6} \left[ R_f x_3 + \omega_o L_f x_4 + V_{dg} - c_3 e_3 L_f + L_f i_{dg}^{ref} \right] \quad (61)$$

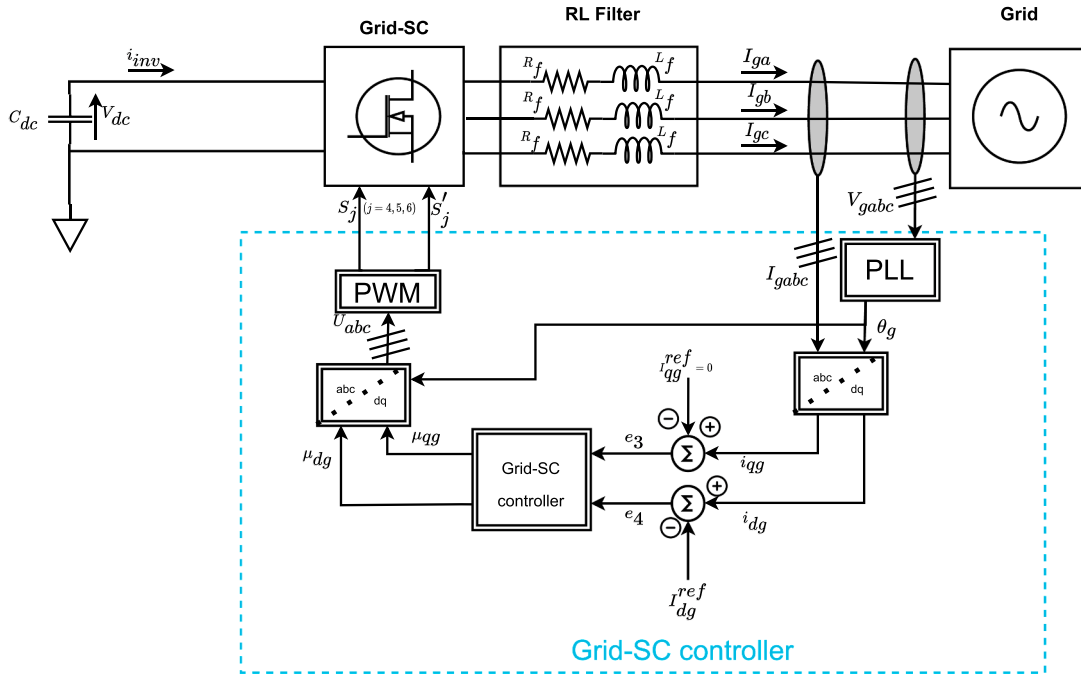


Fig. 7. Grid-SC control structure.



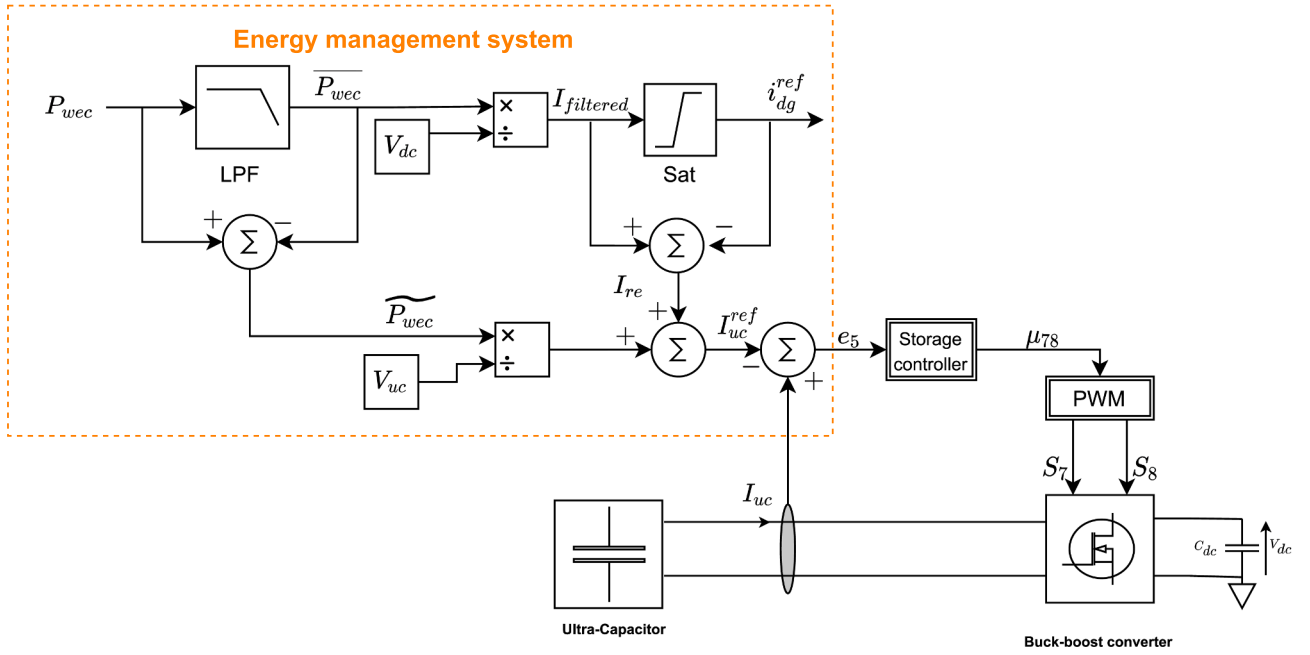


Fig. 8. Energy management system and storage control structure.

$$\mu_{qs} = \frac{1}{x_6} \left[ \omega_o L_f x_3 + R_f x_4 - c_4 e_4 L_f + L_f i_{qs}^{ref} \right] \quad (62)$$

### 3.4. Control of DC/DC converter for UC storage

The control objective for storage converter control is to regulate the DC bus voltage and provide support for the LiTe-Con. Direct DC bus voltage regulation is not possible, due to the non-minimum phase nature of the buck-boost converters used with the ultra-capacitor [65], so an indirect approach is needed here. Specifically, DC bus voltage regulation is achieved by forcing the UC current  $x_5$  to its reference  $I_{uc}^{ref}$ , where  $I_{uc}^{ref}$  is generated through the energy management system (EMS) based on the power balance at the DC bus, as shown in Fig. 8. EMS acts as a supervisory (high-level) control mechanism at the DC bus, ensuring proper reference generation for DC/DC storage converter and Grid-SC controllers. The primary purpose of the EMS is twofold: 1). DC bus voltage regulation and 2). Lite-Con control support. The UC reference current  $I_{uc}^{ref}$ , generated by the EMS, ensures the DC bus voltage regulation and LiTe-Con control support. Furthermore, the EMS also provides a current reference  $i_{dg}^{ref}$  for the Grid-SC controller as shown in Fig. 8.

The power extracted from the WEC  $P_{wec}$  at the DC bus is converted into two components by using a low-pass filter. Filter-based power splitting methods are pretty standard in the literature, especially for HESS applications [66,67]. However, selecting the low-pass filter cut-off frequency (time constant) to maximise the DC bus voltage regulation performance is non-trivial. Given the complex relationship between DC bus voltage regulation and the filter cut-off frequency, the cut-off frequency selection for the EMS is ultimately achieved by trial and error, with minimum DC bus voltage variance achieved with a cut-off frequency of 0.02 [Hz].

$$P_{wec} = \widetilde{P}_{wec} + \overline{P}_{wec} \quad (63)$$

The high-frequency component  $\widetilde{P}_{wec}$  is used to generate a reference for the UC (storage) controller, which absorbs the high frequency fluctuations in  $P_{wec}$  and regulates the DC bus voltage. The saturation block,

shown in Fig. 8, ensures that the negative electrical power (mechanical reactive power) required for the LiTe-Con control is met by the UC storage. The low-frequency (averaged) component  $\overline{P}_{wec}$  of the power is injected into the inverter and used to generate current reference  $i_{dg}^{ref}$  for Grid-SC control.

The following tracking error is defined for UC control:

$$e_5 = x_5 - i_{uc}^{ref} \quad (64)$$

Using Eq. (39), the dynamics of  $e_5$  are derived as:

$$\dot{e}_5 = \frac{V_{uc}}{L_{uc}} - \frac{R_{uc}}{L_{uc}} x_5 - \mu_{78} \frac{x_6}{L_{uc}} - i_{uc}^{ref} \quad (65)$$

To regulate  $e_5$  to zero,  $\dot{e}_5$  is enforced to behave as:

$$\dot{e}_5 = -c_5 e_5 + e_6 \quad (66)$$

where,  $c_5 > 0$  is an additional design parameter.  $e_6$  is now defined as the DC bus voltage error, as follows:

$$e_6 = x_6 - V_{dc}^{ref} \quad (67)$$

The control law  $\mu_{78}$  is easily obtained by comparing Eqs. (65) and (66) as:

$$\mu_{78} = \frac{1}{x_6} \left[ \left( V_{uc} - R_{uc} \right) x_5 + c_5 e_5 L_{uc} - e_6 L_{uc} - L_{uc} i_{uc}^{ref} \right] \quad (68)$$

It is worth mentioning that  $e_6$  is introduced in (68) as an extra damping term to adjust the DC bus voltage. The dynamics of  $e_6$  will be introduced later.

### 3.5. Stability analysis for the complete power conversion system

The stability of the complete power conversion system is established by using Lyapunov stability criteria. In particular, it is investigated that the controllers presented in Eqs. (53), (54), (61), (62), (68) are able to drive the state variations (error) system,  $e_1, e_2, e_3, e_4, e_5,$  and  $e_6$ , to zero.

The system is asymptotically stable if the candidate Lyapunov function  $V(\mathbf{e})$ , with  $\mathbf{e} = [e_1 \ e_2 \ e_3 \ e_4 \ e_5 \ e_6]^T$ , possesses following properties:

$$\begin{cases} V(0) = 0; \\ V(\mathbf{e}) > 0, \quad \forall \mathbf{e} \neq 0; \\ \dot{V}(\mathbf{e}) < 0, \quad \forall \mathbf{e} \neq 0; \end{cases} \quad (69)$$

A typical choice of a candidate Lyapunov function is a quadratic form of state variations (errors  $\mathbf{e}$ ) as  $V(\mathbf{e}) = \frac{1}{2}\mathbf{e}^T\mathbf{Q}\mathbf{e}$ , where  $\mathbf{Q} \in \mathbb{R}^{6 \times 6}$  is a symmetric positive definite matrix. The choice of  $\mathbf{Q}$  provides some degree of freedom in the selection of the candidate Lyapunov function; however, an energy-like Lyapunov function is preferred [68]. For simplicity, we consider  $\mathbf{Q} = \mathbf{I} \in \mathbb{R}^{6 \times 6}$ , which results in the following energy-like quadratic Lyapunov function for the complete power conversion system.

$$V(\mathbf{e}) = \frac{1}{2}(e_1^2 + e_2^2 + e_3^2 + e_4^2 + e_5^2 + e_6^2). \quad (70)$$

It is clear that the  $V(\mathbf{e})$  satisfies the first three stability properties expressed in (69). The fourth property in (69) can be satisfied by using the control laws obtained in Eqs. (53), (54), (61), (62), and (68). For the system to be asymptotically stable,  $\dot{V}(\mathbf{e})$  must be negative definite, i.e.  $\dot{V}(\mathbf{e}) < 0$ . Taking the derivative of Eq. (70), yields:

$$\dot{V}(\mathbf{e}) = (e_1\dot{e}_1 + e_2\dot{e}_2 + e_3\dot{e}_3 + e_4\dot{e}_4 + e_5\dot{e}_5 + e_6\dot{e}_6) \quad (71)$$

Substituting expressions for  $\dot{e}_1, \dot{e}_2, \dot{e}_3, \dot{e}_4$ , and  $\dot{e}_5$  from (51), (52), (59), (60) and (66), respectively, into (71) results in the following:

$$\dot{V}(\mathbf{e}) = -c_1e_1^2 - c_2e_2^2 - c_3e_3^2 - c_4e_4^2 - c_5e_5^2 + e_6(e_5 + \dot{e}_6) \quad (72)$$

To verify that  $\dot{V}(\mathbf{e}) < 0$ ,  $\dot{e}_6$  is defined as follows:

$$\dot{e}_6 = -c_6e_6 - e_5 \quad (73)$$

where  $c_6 > 0$  is yet another design parameter. Using (66),  $\dot{V}(\mathbf{e})$  is updated as:

$$\dot{V}(\mathbf{e}) = -c_1e_1^2 - c_2e_2^2 - c_3e_3^2 - c_4e_4^2 - c_5e_5^2 - c_6e_6^2 \quad (74)$$

Eq. (74) shows that  $\dot{V}(\mathbf{e}) < 0$ ; hence, asymptotically stability of the equilibrium  $[e_1, e_2, e_3, e_4, e_5, e_6]^T = [0, 0, 0, 0, 0, 0]^T$ , is achieved. It is worth mentioning that regulation of the DC bus voltage  $V_{dc}$  is achieved indirectly by controlling UC current  $i_{uc}$ . In particular, the convergence of error  $e_6$  depends upon the convergence of  $e_5$  and the introduction of  $e_6$  puts an indirect constraint on the  $e_5$ . To validate Eq. (73),  $V_{dc}^{ref}$  is generated using Eq. (40) as follows:

$$V_{dc}^{ref} = \int \left[ c_6e_6 + e_5 + \frac{1}{C_{dc}}(\mu_{ds}x_1 + \mu_{qs}x_2 + \mu_{78}x_5 - i_{inv}) \right] \quad (75)$$

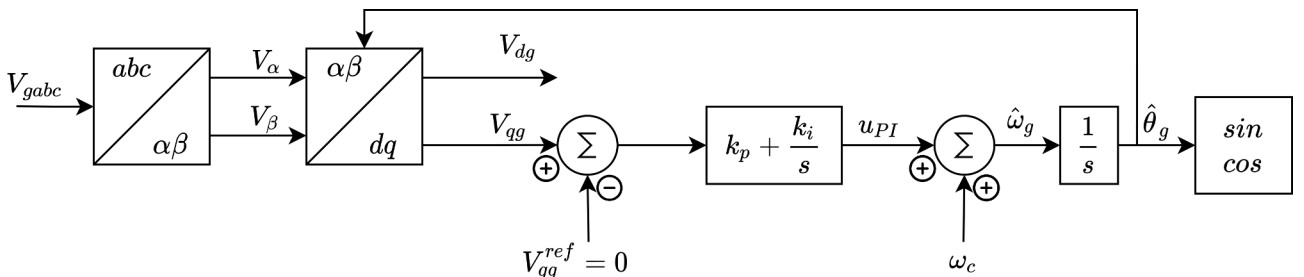


Fig. 9. SRF-PLL structure for grid phase tracking.

#### 4. Grid Synchronisation and phase-locked loop

A PLL is a closed-loop feedback control system that synchronises its output signal with the reference input signal in frequency and phase. In our study, a PLL is used to estimate the grid frequency and phase. Ideal grid conditions are assumed, i.e. the grid is assumed to be a sinusoidal voltage source with constant frequency. A synchronous reference frame PLL (SRF-PLL) is employed here due to its simplicity and accuracy for estimating the grid phase under ideal grid conditions [69]. The structure of a SRF-PLL is shown in Fig. 9.

The following input grid voltages are assumed:

$$\begin{aligned} v_{ga} &= V_g \sin(\theta_g) \\ v_{gb} &= V_g \sin\left(\theta_g - \frac{2\pi}{3}\right) \\ v_{gc} &= V_g \sin\left(\theta_g - \frac{4\pi}{3}\right) \end{aligned} \quad (76)$$

where  $V_g$  and  $\theta_g$  are the amplitude and phase of three-phase grid voltages, respectively. Using the Park and Clarke transformations, the  $d$ -axis voltage  $V_{dg}$  is aligned with  $V_g$ , and  $V_{qg}$  is orthogonal to the  $d$ -axis.  $V_{qg}$  then contains phase error information which is regulated by a PI controller.

$$G_c(s) = \frac{k_p s + k_i}{s} \quad (77)$$

The output of the PI controller  $u_{PI}$  is an actuation signal which is added to the centre frequency  $\omega_c$ . The outcome of the second sum block in Fig. 9 is the estimated frequency in radians, which is applied to the voltage controlled oscillator to provide an estimate of the phase angle  $\hat{\theta}_g$ . The closed-loop transfer function of the PLL system is obtained as:

$$G_{CL}(s) = \frac{V_g(k_p s + k_i)}{s^2 + V_g k_p s + V_g k_i} \quad (78)$$

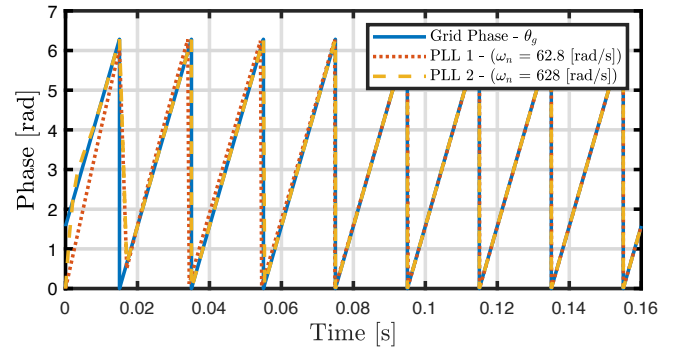


Fig. 10. Grid phase tracking performance comparison of two SRF-PLLs with different bandwidths..

The closed-loop transfer function  $G_{CL}(s)$  in (78) can be represented as a second-order transfer function of the form:

$$G_{CL}(s) = \frac{2\zeta\omega_n s + \omega_n^2}{s^2 + 2\zeta\omega_n s + \omega_n^2} \quad (79)$$

with,

$$\omega_n = \sqrt{V_g k_i}, \text{ and } \zeta = \frac{V_g k_p}{2\sqrt{V_g k_i}}$$

where  $\omega_n$  is the bandwidth of the closed-loop PLL system, and  $\zeta$  is the damping ratio. The controller gains in Eq. (77) are tuned to minimise the phase error, which is the main objective of the PI controller. The PI controller shown in Fig. 9 acts as a low-pass filter to reduce measurement noise. The design criteria for the SRF-PLL PI controller is a trade-off between fast-tracking and measurement noise rejection. Increasing the PLL bandwidth will result in a faster response time at the cost of poor filtering ability. Fig. 10 shows the performance comparison for two SRF-PLLs with different bandwidths, namely PLL 1, with a bandwidth of 62.8 [rad/s], and PLL 2, with a bandwidth of 628 [rad/s]. It is clear, from Fig. 10, that the grid phase tracking performance of PLL 2, with the lower settling time, is much better than PLL 1. Hence, increasing the bandwidth of SRF-PLL results in improved phase tracking performance, which is the main purpose of the SRF-PLL. Here, the selected bandwidth is  $\omega_n = 628$  [rad/s] with the gains of the loop filter are calculated from (78) and (79) as  $k_p = 2.22$  and  $k_i = 985.96$ .

## 5. Results and Discussion

The performance of the proposed W2G control scheme is evaluated in simulation using the MATLAB/Simulink environment.

An irregular wave model is considered in this study, which is used to generate excitation force time traces  $f_{exc}(t)$ , from the free-surface elevation  $\eta(t)$ , based on a JONSWAP spectrum  $S_\eta(\omega)$  [70]. The free-surface elevation  $\eta(t)$  is generated from a white noise signal, filtered according to the wave spectrum  $S_\eta(\omega)$  [71]. The sea-state parameters characterising the spectrum are as follows: a fixed significant wave height  $H_s = 2$  m, peak period in the interval  $T_p \in [5, 12]$  s, and peak enhancement factor  $\gamma = 3.3$ . Fig. 11 shows the spectrum  $S_\eta(\omega)$  for peak periods  $T_p = \{5, 6.4, 7.8, 9.2, 10.6, 12\}$  s.

In this study, we consider a state-of-the-art CorPower-like WEC, oscillating in heave, which represents one of the most established and standard current WEC designs in wave energy development [59,72]. Fig. 12 illustrates the CorPower-like device, considered in this study, with most relevant physical dimensions shown.

Fig. 13 shows the frequency response mappings associated with the LiTe-Con. Specifically, the left column of the Fig. 13 shows  $K_{ff}^{LC}(\omega)$ , along

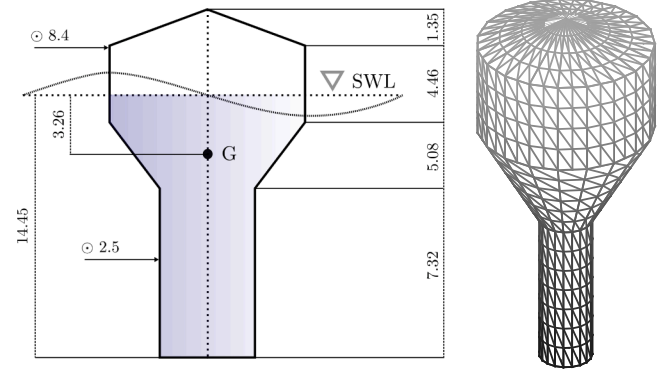


Fig. 12. Full-scale CorPower-like device considered in this case study. Dimensions are in metres. The acronym SWL stands for still water level and the letter G is used to denote the center of gravity of the device.

with the optimal (target) feedforward controller mapping  $K_{ff}^{opt}(\omega)$ . In addition, the right side of Fig. 13 depicts the overall system force-to-velocity mapping for controller  $T_{exc \rightarrow v}^{LC}(\omega)$  along with the optimal (target) force-to-velocity response  $T_{exc \rightarrow v}^{opt}(\omega)$ . The shaded region in Fig. 13 represents the frequency range selected for controller synthesis. Furthermore, the effect of changing  $k$ , for constraint handling, is illustrated on both frequency response mappings. The device motion (displacement) is constrained to the operational space  $[-1.5, 1.5]$  m. The excitation force in operational conditions is immeasurable, and therefore, it has to be estimated. In general, the future knowledge of excitation force is required for the majority of energy maximising WEC controllers, which would be provided by excitation force estimation and forecasting methods. The prediction requirements for a real-time WEC controller are documented in [73], and a critical review of various excitation force estimators is presented in [74]. For constrained LiTe-Con case, the values of  $k$  are determined by exhaustive simulations for each sea state considered. Hence, full knowledge of excitation force is assumed, for this case. For each sea-state with peak periods  $T_p \in [5, 12]$  s, the resulting optimised  $k$ , which maintain operation with the device physical constraints, values are shown in Fig. 14.

In the following part of this section, plots for absorbed power, converted power, peak-to-average power (PTAP) ratio for converted power, and maximum PTO force, are presented for the range of wave periods considered, i.e.  $T_p \in [5, 12]$  s. The absorbed hydrodynamic power is the mechanical output of the WEC, and the converted power is the electrical power converted by the PTO mechanism and measured at the Gen-SC output. To determine statistically relevant results, the results are averaged over ten realisations of each sea-state considered.

The results obtained with LiTe-Con are compared with resistive

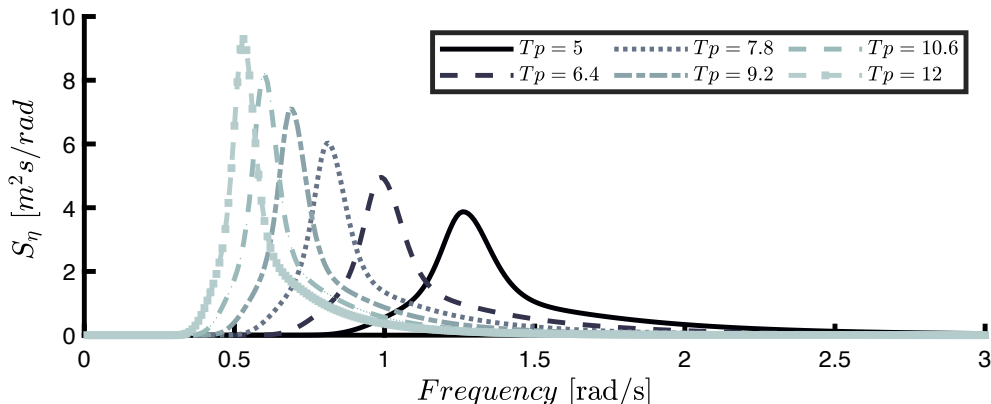
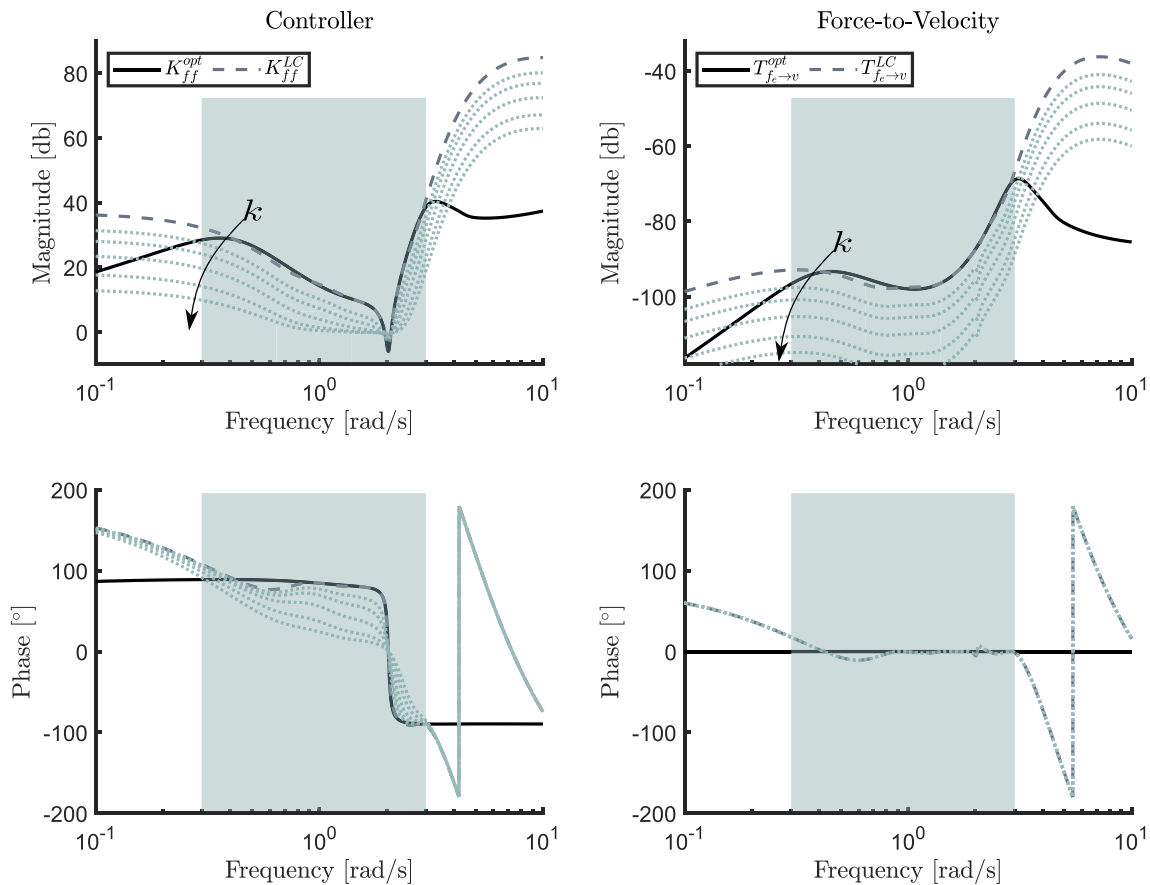
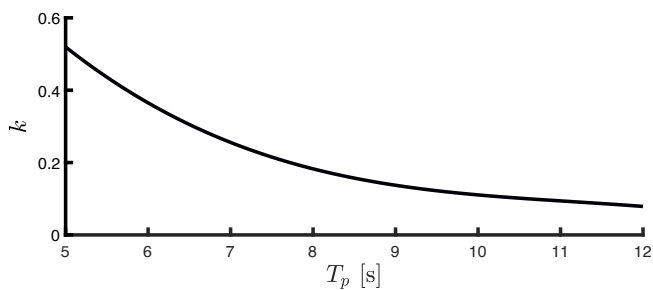


Fig. 11.  $S_\eta(\omega)$  for peak periods  $T_p = \{5, 6.4, 7.8, 9.2, 10.6, 12\}$  s.



**Fig. 13.** Frequency–response mappings of the LiTe-Con. In particular, the left column illustrates  $K_{ff}^{LC}(\omega)$  (dashed line), together with the optimal feedforward mapping  $K_{ff}^{opt}(\omega)$  (solid line). The right column depicts the force-to-velocity mapping associated with the LiTe-Con, i.e.,  $T_{fc \rightarrow v}^{LC}(\omega)$  (dashed line), along with the optimal force-to-velocity frequency response  $T_{fc \rightarrow v}^{opt}(\omega)$  (solid line). The effect of the constraint handling mechanism for  $k$  in the set of  $\{0.58, 0.4, 0.24, 0.13, 0.080\}$ , is depicted with dotted lines.



**Fig. 14.** Optimised  $k$  values for sea states with peak periods  $T_p \in [5, 12]$  s.

loading (passive damping) control, predominant in the literature regarding grid integration of WECs, in Fig. 15. In particular, Fig. 15(a) shows the absorbed hydrodynamic power for both controllers for  $T_p \in [5, 12]$  s. In Fig. 15(a), LiTe-Con is shown to significantly outperform the passive damping controller since the LiTe-Con is a broadband reactive hydrodynamic controller i.e. it effectively achieves device resonance at a broader range of wave frequencies. Fig. 15(b) shows that, as a result, the converted power is also greater for LiTe-Con than for passive damping control. However, at larger periods ( $T_p > 10$  s), the converted power for the LiTe-Con drops significantly, due to the increased Cu-losses in the PTO (LPMG). This phenomenon is not unique to this study and has been previously reported in the literature, e.g., in [25,75,76]. At higher periods, the LiTe-Con requires higher peak PTO forces, which causes an increase in stator currents of the LPMG. Hence, a dramatic increase in

the losses at higher periods, to which there are a number of potential solutions. One solution is to employ a global W2G control, which has concurrent knowledge of all system components and finds the best compromise to maximise grid power. Another solution, based on the idea of control co-design, would be to optimise the position of the device resonant frequency (relative to predominant wave spectral peak) to minimise control action. A possible further solution is adding constraints on peak PTO force and stator currents in the WEC hydrodynamic control formulation as, for example, in [77]. An alternative solution is to use a rotary generator, such as DFIG or PMSG, etc., with an appropriate rectifying gearing mechanism for example, see [78], to increase rotor speeds and reduce peak PTO forces. However, adding a gearing mechanism may result in additional frictional losses. However, these refinements are beyond the current paper scope, but may be considered in future studies. In the case of passive damping control, the losses also increase for higher periods, but not as significantly as in the case of LiTe-Con. PTAP ratios for the converted power are presented in Fig. 15(c), which shows that PTAP ratios for passive damping control average around 10, which are consistent with this type of controller [76]. In contrast, for the constrained LiTe-Con case, the PTAP ratios are more than double those for passive damping control at periods  $T_p < 10$  s. For periods  $T_p > 10$  s, PTAP ratios increase significantly and increase to 50, at the highest period  $T_p = 12$  s. The high peak force requirement can also explain the higher PTAP ratios at larger periods for LiTe-Con. Although the PTAP ratios for LiTe-Con at lower periods under panchromatic waves are slightly higher than findings in [23,33], the PTO mechanisms used in [23,33] are different from the LPMG used for our case, which may have some impact on the PTAP ratios. It is also

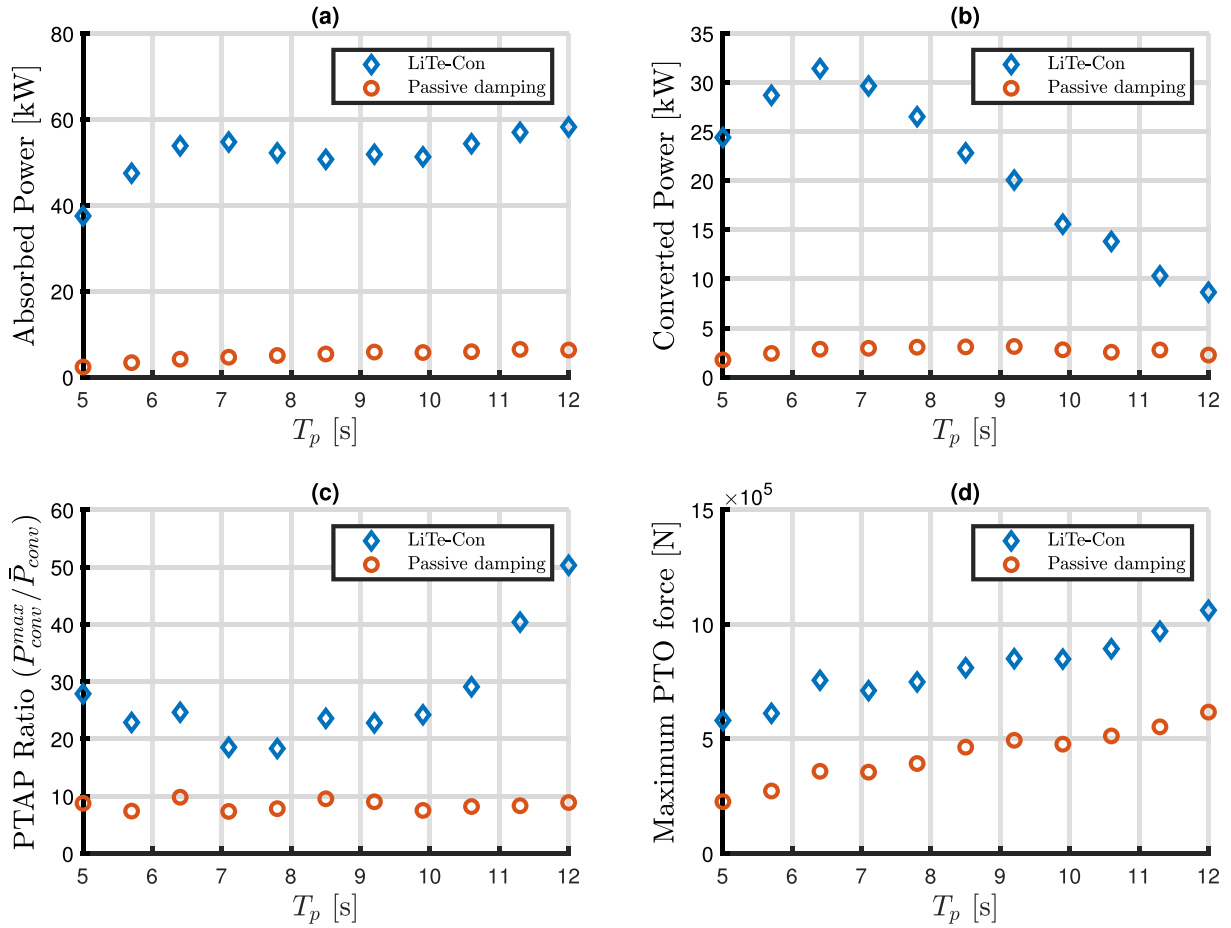


Fig. 15. Performance comparison of LiTe-Con and Passive damping control for the totality of sea-states considered. (a) Absorbed hydrodynamic power [kW] (b) Converted power [kW] (c) PTAP ratio for converted power (d) Maximum PTO (control) force [N].

worth mentioning that the lowest PTAP ratios are around the natural period ( $\approx 6.5$  s) of the device since the hydrodynamic controllers for point absorber WECs require minimal control action close to the natural period of the device. Fig. 15(d) provides the comparison for the maximum control force required by both controllers, at each period considered, showing that the maximum control force for the LiTe-Con is significantly larger than the passive damping control, as expected, due to its broadband reactive nature.

Fig. 16 shows the efficiencies of the various stages of the power train under both passive and LiTe-Con controllers.  $\eta_{mech}$ ,  $\eta_{PTO}$ ,  $\eta_{W2W}$  and  $\eta_{W2G}$  represent the device's mechanical efficiency, PTO efficiency, W2W efficiency, and W2G efficiency, respectively. In particular, Fig. 15(a) presents the mechanical efficiency  $\eta_{mech}$ , which clearly shows that the mechanical efficiency is much higher for LiTe-Con, as compared to passive hydrodynamic control, due to the higher power absorption capability of broadband LiTe-Con control. Additionally, it is also clear from Fig. 16(a) that the mechanical efficiency for LiTe-Con decreases, especially at periods  $T_p > 7$ , due to the action of constraint handling mechanism, which restricts device motion to within physical operation range. Fig. 16(b) shows the PTO (LPMG) efficiency  $\eta_{PTO}$ , for the range of wave periods considered, and it is clear that the  $\eta_{PTO}$  for passive control is consistently better than that for LiTe-Con. The reason for such behaviour is the Cu-losses in the LPMG stator, which are much higher for LiTe-Con than for passive control. The W2W efficiency  $\eta_{W2W}$  is presented in Fig. 16(c), and, as expected, the W2W efficiency is better for LiTe-Con due to overall better power absorption performance. For wave periods  $T_p < 7$ , the W2W efficiencies achieved (50–60 %) for the LiTe-Con are close to the efficiencies achieved by the authors in [23,33]. Additionally,  $\eta_{W2W}$  is superior to the efficiency presented in [31], which uses a

hydraulic PTO mechanism and achieves a  $\eta_{W2W}$  of around 8%. However, it is essential to mention that the hydraulic PTO mechanism includes a power conditioning mechanism, which provides much better output power quality than a direct drive PTO. For periods  $T_p > 7$ , the W2W efficiency drops significantly due to two main reasons. Firstly, the drop in  $\eta_{mech}$ , due to the action of constraint handling mechanism. Secondly, the decreased  $\eta_{PTO}$ , due to increased Cu-losses associated with higher peak currents at higher wave periods. Fig. 16(d) presents W2G efficiency calculated using averaged grid power at each sea state. For a direct drive heaving WEC controlled with LiTe-Con, it can be concluded from Fig. 16 that the reasonable efficiencies are achievable as long as the wave periods are close to the natural period of the device ( $\approx 6.5$  s) and control action (PTO force  $f_{pto}$ ) is light.

Naturally, the increased power capture performance of the LiTe-Con comes with some capital costs increases. First of all, the increased PTO force requirement directly influences the required LPMG rating, which increases the PTO cost. In addition, higher PTAP values, especially at higher wave periods, also require higher ratings for the power conversion and storage systems. These factors increase equipment costs in the power train, leading to a higher capital cost. Though beyond the scope of this study, we note that optimisation-based controllers such as MPC can (more elegantly) incorporate maximum PTO force constraints and Cu-losses in the problem formulation, hence reducing both the PTO force requirements and PTO losses [25], but with additional computational expense. In terms of costs, optimisation-based controllers such as MPC can maximise the economic benefit by implementing constraints on peak PTO force, reactive power and stator current requirements, assuming the availability of W2G model, which may result in lower Cu-losses and equipment ratings (capital costs). However, this formulation



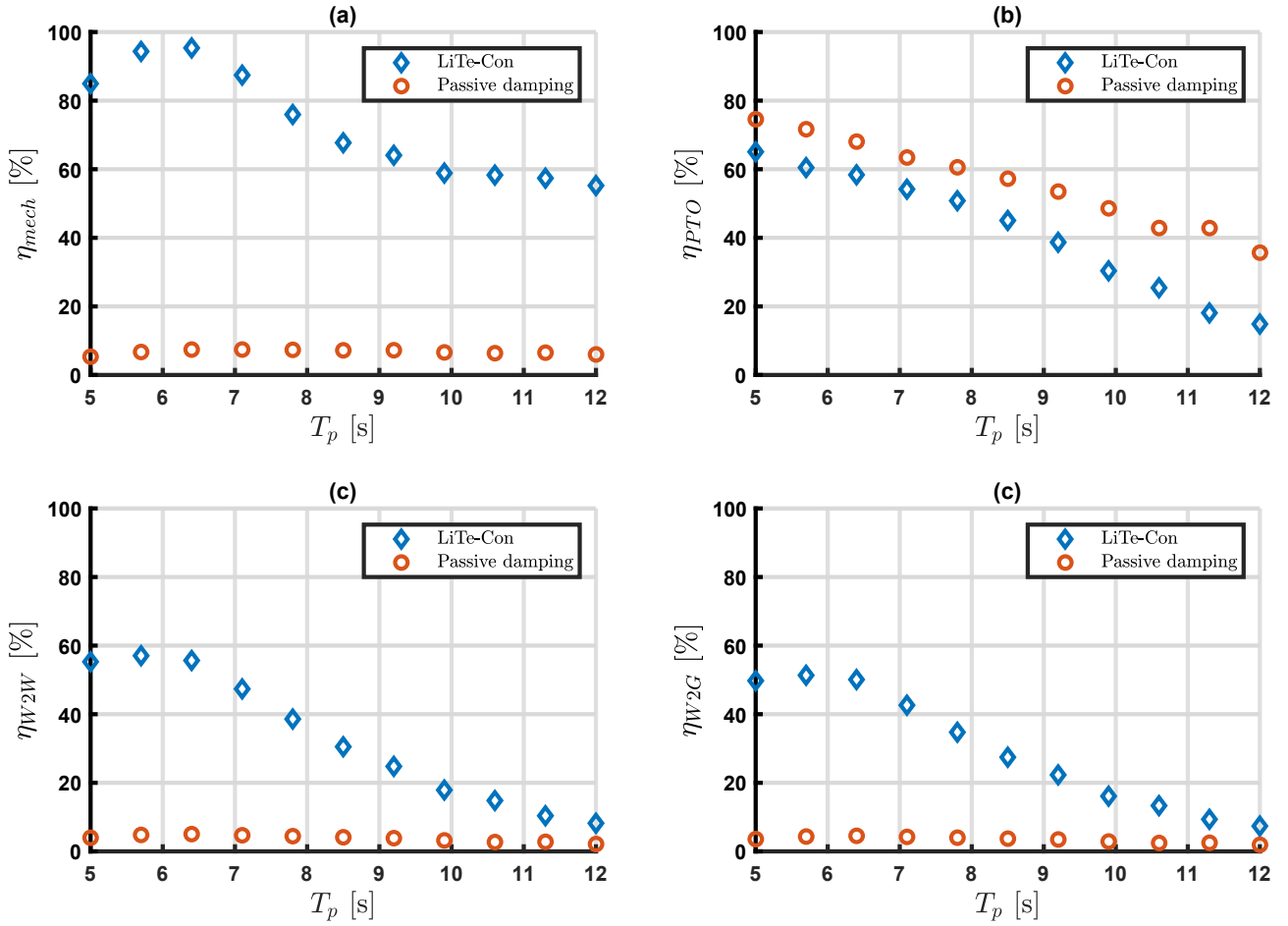


Fig. 16. Efficiency plots of LiTe-Con and Passive damping control for various power train stages (a) Mechanical efficiency  $\eta_{mech}$  [%] (b) PTO efficiency  $\eta_{PTO}$  [%] (c) W2W efficiency  $\eta_{W2W}$  [%](d) W2G efficiency  $\eta_{W2G}$  [%].

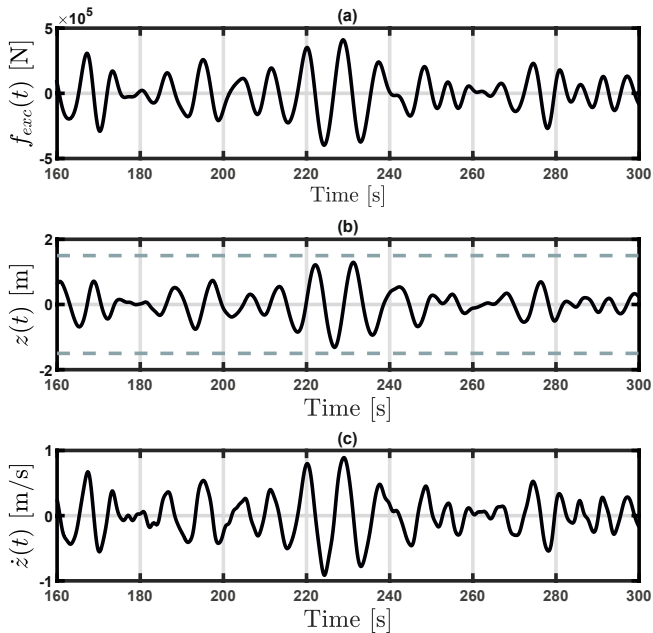


Fig. 17. Time series plots of WEC dynamics under constrained LiTe-Con (a) Excitation force [N] (b) Device displacement (solid line) and displacement constraint (dashed line) [m] (c) Velocity [m/s].

can lead to a nonlinear constraint optimisation problem [79] that may not be well suited for real-time implementation, due to the increased computational costs. There is a trade-off between the performance, constraint handling, and, more importantly, the power train equipment costs.

The constraint handling performance of the LiTe-Con and the tracking performance of the Lyapunov power converter controllers are assessed here using time series plots for a single sea state. The properties of the considered sea state are  $T_p = 8.5$  s (which is obtained as the average between the extreme of the complete wave period range, i.e. [5,12] s) and  $H_s = 2$  m. The results presented in this section include constrained LiTe-Con control with displacement constraint of  $z_{max} = 1.5$  m on the hydrodynamic side.

Fig. 17 (a), (b) and (c) shows the excitation force, heave excursions (displacement) and velocity, respectively. Fig. 17 (b) illustrates that the LiTe-Con satisfies the motion constraints (indicated with the dashed lines), i.e. the device motion is contained in the physical operation range, which is one of the benefits of using this approach. The Lyapunov-based Gen-SC controller tracking performance is shown in Fig. 18 (a), (b) and (c), which confirms that the PTO force reference provided by the LiTeCon is perfectly tracked by the PTO force  $f_{pto}(t)$ , by regulating the LPMG stator q-axis current  $x_2(t)$  to its reference  $i_{qs}^{ref}(t)$ . Furthermore, generator Cu-losses are minimised by regulating the d-axis current  $x_1(t)$  to zero. On the other hand, Fig. 18 (a), (b) and (c) also show the tracking performance of an alternative PI controller, which struggles to track the reference signals compared with the Lyapunov control. Despite the good tracking performance of the Lyapunov control, the control objective of extracting maximum power from the waves depends heavily upon how

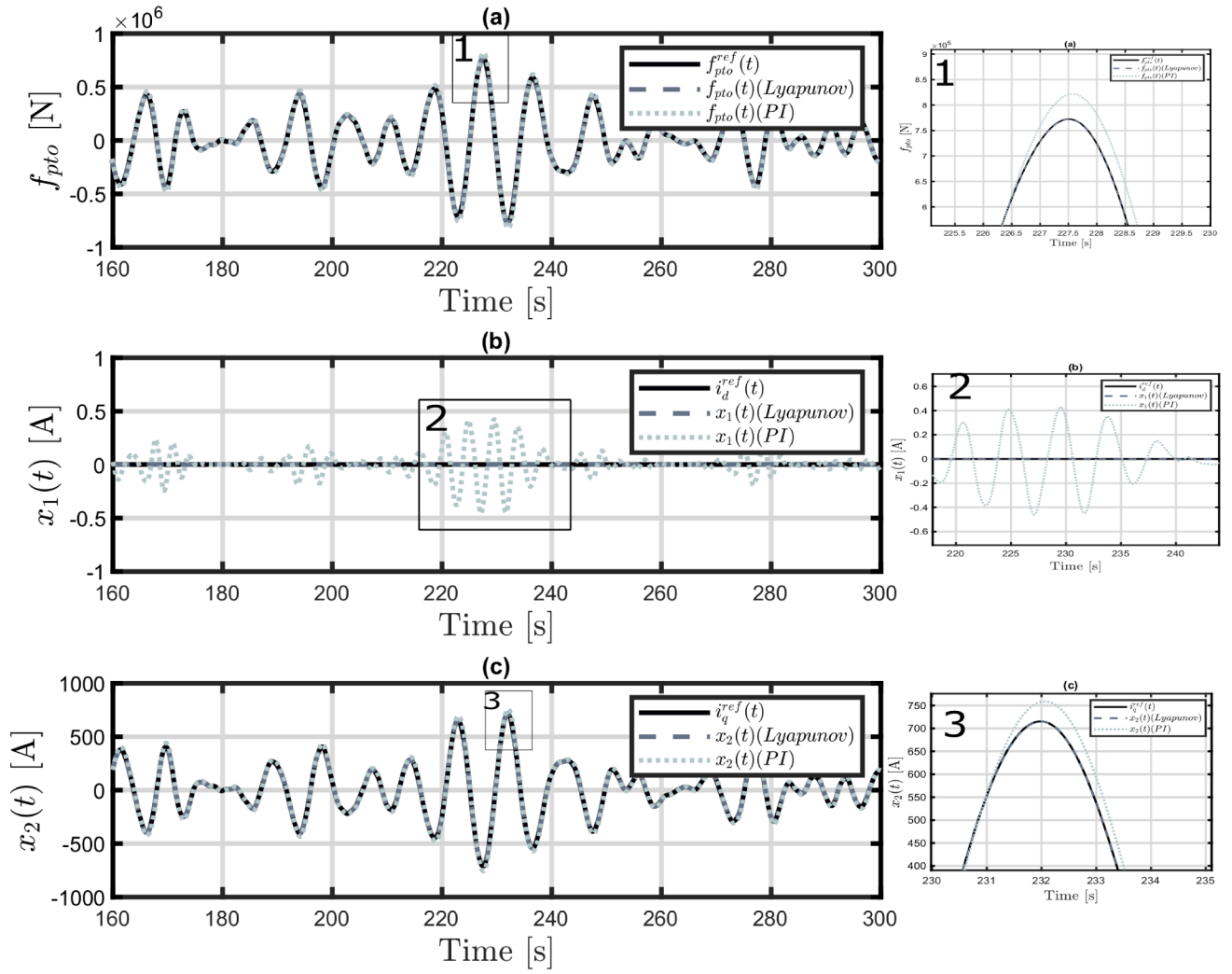


Fig. 18. Tracking performance of the Gen-SC controller (a) PTO force [N] (b) d-axis stator current [A] (c) q-axis stator current [A].

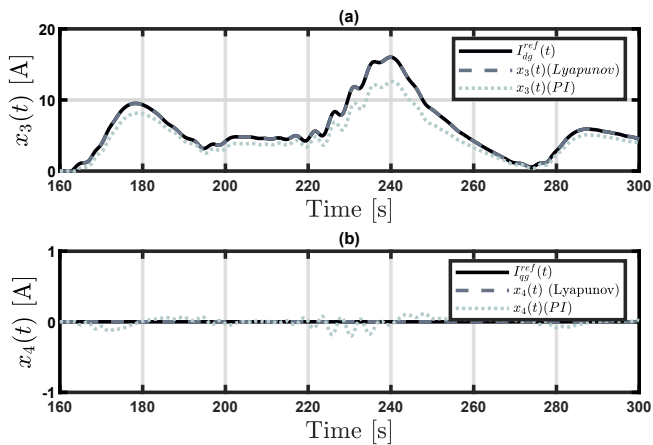


Fig. 19. Tracking performance of the Grid-SC controller (a) d-axis current [A] (b) q-axis current [A].

good a PTO force reference  $f_{pto}^{ref}$  the hydrodynamic control produces. This is depicted in Fig. 15, which shows that the power absorbed is always less for a passive damping controller compared to LiTeCon, regardless of the type of controller used for the power converters.

The tracking performance of the Grid-SC control is presented in Fig. 19. Both  $d$ -axis and  $q$ -axis currents are tracked perfectly and errors are minimised by Lyapunov control. Fig. 19 also shows significant degradation in tracking performance when using an alternative PI controller, primarily due to an inability to handle system nonlinearities. The maximum active power injection is achieved by tracking the  $d$ -axis current  $x_3(t)$  to its reference  $i_{dg}^{ref}$ , which is generated by the energy management system at the DC bus. Fig. 19(a) shows that the injected current varies according to the wave profile. On the other hand, electrical reactive power injection is zero due to the regulation of  $q$ -axis current  $x_4(t)$  to zero, resulting in a unity power factor for the injected grid power. In addition, the tracking performance of the storage controller is shown in Fig. 20. Fig. 20(a) shows that the UC storage absorbs high frequency power components at the DC bus, allocated through the EMS. Once again, the Lyapunov controller significantly outperforms the PI controller in terms of tracking ability and achieves much tighter DC bus voltage regulation, as shown in Fig. 20. Tight DC bus voltage regulation is achieved indirectly through the control of the UC storage current  $x_5(t)$ , as presented in Fig. 20(b). The addition of the UC system both increases the captured power (by facilitating reactive control), as well as improving the quality (reducing the variability) of the supplied grid power, therefore justifying the additional cost of the UC system. The W2G systems are actuated by incoming panchromatic waves, which are dynamic at all times. The wave excitation force, presented in Fig. 17(a), is calculated from the wave elevation time series

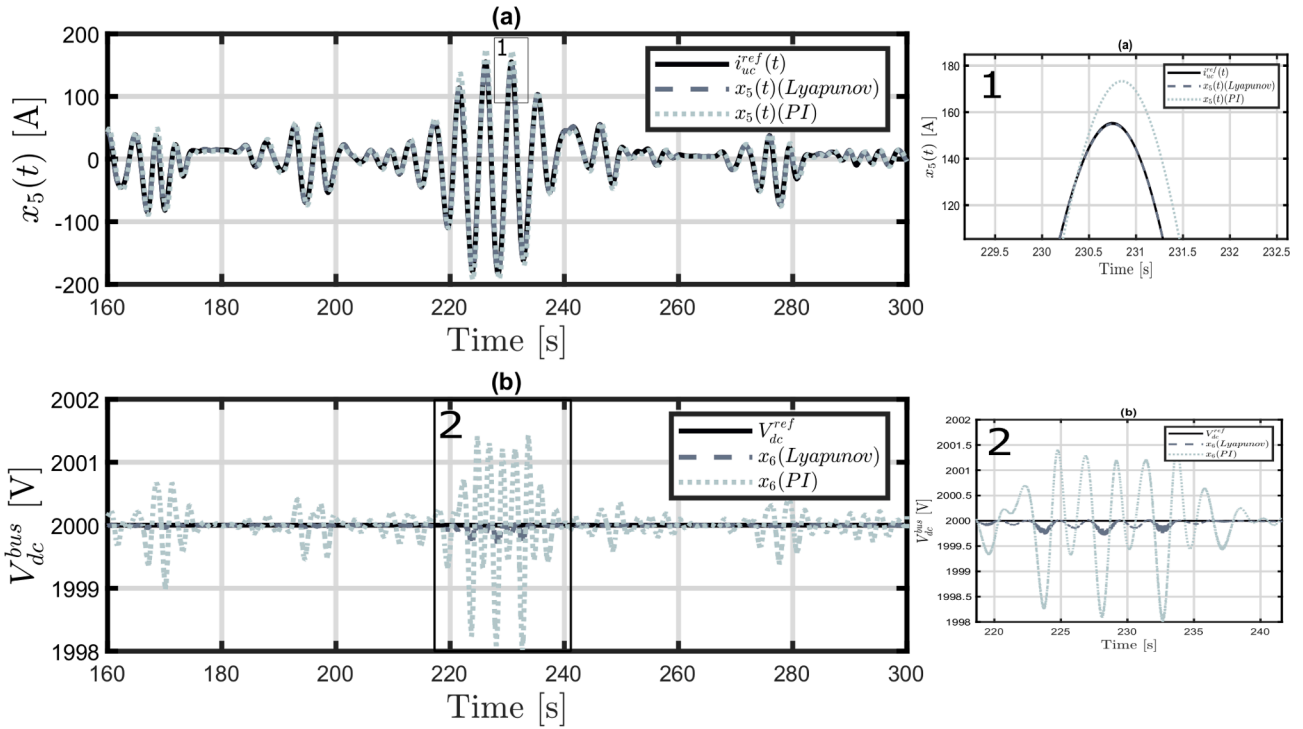


Fig. 20. Tracking performance of the UC storage controller (a) Ultra-capacitor current [A] (b) DC bus voltage [V].

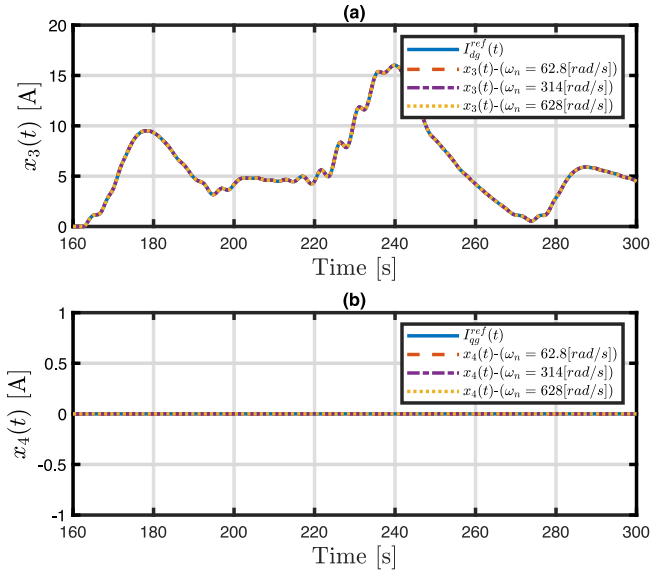


Fig. 21. Tracking performance of the Grid-SC controller for different PLL bandwidths (a) d-axis current [A] (b) q-axis current [A].

derived from the wave spectrum shown in Fig. 11. Therefore, the results shown in Figs. 17–22 illustrate the satisfactory dynamic performance of the power converter controllers due to the ever-changing wave excitation force, making the complete W2G system dynamic throughout the operation. However, the system is not required to respond to any sudden changes in the wave excitation due to its smooth frequency domain (Fourier) nature. The grid is assumed to be a three-phase balanced voltage source with regular operation on the grid side. The operation of the proposed system during grid faults and fault-ride through capabilities (FRT) are not considered in this study and will be the subject of future research.

In addition, changing the PLL bandwidth does not affect the tracking

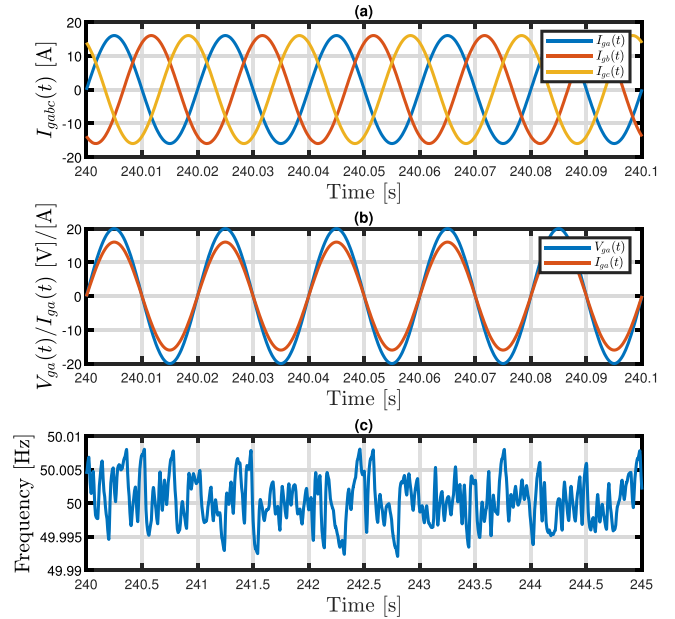
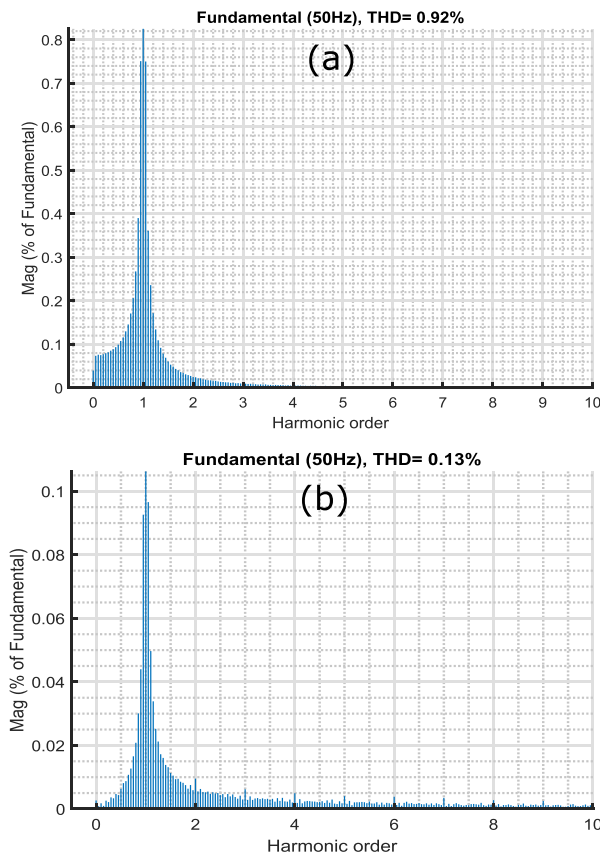


Fig. 22. Power quality plots (a) Three-phase injected current [A] (b) Scaled Phase A grid voltage [V] and Phase A current [A] (c) Frequency variations [Hz].

performance of proposed Lyapunov controllers due to the ideal grid conditions assumed in this study, resulting in identical control results for different PLL bandwidths. For example, Fig. 21 illustrates the identical tracking performance of the Grid-SC controllers for various PLL bandwidths. Similar results can be obtained for Gen-SC and storage controllers but are omitted for brevity. However, the PLL bandwidth may cause harmonic resonance, or even instability in grid-connected inverter (Grid-SC) systems under weak grid conditions due to the coupling between the PLL and the grid impedance, as described in [80,81].

The quality of injected power is illustrated in Fig. 22, with Fig. 22(a)



**Fig. 23.** Harmonic spectrum (a) Magnitude of grid current harmonics (b) Magnitude of grid voltage harmonics.

showing the three-phase grid currents. Fig. 22(b) confirming that the Phase A grid voltage (scaled down) and current are in phase with each other, which guarantees unity power factor. Grid power frequency excursions are presented in Fig. 22(c), which shows that the frequency remains under the contingency band  $50 \pm 0.5$  Hz, as specified by the Irish grid codes. Furthermore, the grid voltage and current harmonics for Phase A are shown in Fig. 23. Under IEEE Standard 519–1992 [82], the maximum allowable THD level for grid voltage and current is 5%. It is clear from Fig. 23 that the harmonics for current (0.92%) and voltage (0.13%) are well below the limits set by the Standard 519–1992. Therefore, the proposed W2G system is grid compliant and provides good power quality.

## 6. Conclusions

In this paper, a W2G system is modelled, and a high-performance W2G control scheme is designed for a direct drive heaving point absorber WEC. The motivation for this W2G control approach lies in the identification of conflicts that arises at various stages of the power train. On the device side, multi-frequency reactive LiTe-Con hydrodynamic control is used. In particular, the LiTe-Con provides more power extracted from waves than passive damping control and provides a position constraint handling mechanism required for device safety. Although the LiTe-Con delivers more power than passive damping control, there are some implications of using LiTe-Con regarding

equipment ratings and costs. The mechanical reactive power requirements of LiTe-Con, and higher PTAP ratios (especially at higher wave periods) of the converted power, increase the rating requirements of the PTO and power conversion equipment in the power train. There is a case to be made to limit the amount of mechanical reactive (negative electrical) power to the WEC from the DC link, given the implications for device rating. However, this represents a nonlinear constraint and significantly increases the control complexity. For the class of ‘simple’ WEC controllers [60], constraint handling is kept to a low level of complexity. Still, there are some possibilities with more complex controllers such as pseudo-spectral and MPC [79,83] at the cost of computational complexity.

Lyapunov-based nonlinear controllers are used for the power converters’ control in the power train and perform well under various operating conditions. In addition, the use of a Lyapunov-based control synthesis procedure *guarantees* the stability of the electrical component of the power train. Furthermore, an EMS system is also added at the DC bus for tight DC bus voltage regulation and to provide for the mechanical reactive power requirements of LiTe-Con, via an ultra-capacitor storage system. The proposed W2G control scheme also ensures that the power quality standards such as power fluctuations, frequency variations and THD levels remain well within limits set by typical grid codes and IEEE standards.

The proposed approach can be straightforwardly applied to the other WEC devices, especially on the grid-side of the power train; however, on the device side, different WECs respond differently under controlled conditions. The proposed scheme also provides a starting point for studies in which wave energy is combined with other renewable energy modalities such as wind and solar, by adding them at the DC bus, including for microgrid applications. In such applications, long term storage such as battery storage would also be required to further enhance the value of wave energy delivered, which will be the subject of future research.

## CRedit authorship contribution statement

**Hafiz Ahsan Said:** Conceptualization, Methodology, Investigation, Formal analysis, Software, Writing - original draft, Writing - review & editing, Visualization. **Demián García-Violini:** Methodology, Formal analysis, Software, Writing - review & editing. **John V. Ringwood:** Conceptualization, Writing - review & editing, Supervision, Funding acquisition, Project administration.

## Declaration of Competing Interest

The authors declare that they have no known competing financial interests or personal relationships that could have appeared to influence the work reported in this paper.

## Acknowledgement

Thanks are due to CarrieAnne Barry of the Centre for Ocean Energy Research (COER) at Maynooth University for providing language help and proofreading the article. This work is supported by COER and the Dept. of Electronic Engineering, Maynooth University, and by Science Foundation Ireland through the Marine Renewable Ireland (MaREI) Centre under Grant 12/RC/2302\_P2. Demián García-Violini is supported by the Universidad Nacional de Quilmes.

## Appendix A. System Parameters

**Table A1**

W2G system parameters for the simulation study.

WEC	
Total mass	$1.4646 \times 10^5$ kg
Hydrostatic stiffness $K_{hs}$	$5.5724 \times 10^5$ N/m
LPMG and Gen-SC	
Stator Resistance $R_s$	0.29 $\Omega$
Stator inductance $L_s$	0.03 H
Flux linkage $\psi_{PM}$	23 Wb
Pole pitch $\tau$	0.1 m
Controller gains	$c_1 = 10, c_2 = 1 \times 10^2$
Grid and Grid-SC	
Filter Resistance $R_f$	0.15 $\Omega$
Filter inductance $L_f$	0.2 H
Controller gains	$c_3 = 9 \times 10^2, c_4 = 1 \times 10^2$
Grid frequency $f_g$	50 Hz
UC and DC/DC converter	
Supercapacitor voltage $V_{sc}$	1280 V
Inductance $L_{sc}$	3.3 mH
ESR $R_{sc}$	20 m $\Omega$
Controller gain	$c_5 = 9 \times 10^2$
DC bus	
Voltage $V_{dc}^{ref}$	2000 V
Capacitance $C_{dc}$	4 mF

## Appendix B. Passive damping control

For comparison, a passive control, also known as resistive loading (RL) control, is used to generate the PTO reference force on the device-side. The PTO reference force  $f_{pto}^{ref}$  generated from a RL control [25] is given by:

$$f_{pto}^{ref} = |Z(\omega_{pk})| \dot{z} \quad (B.1)$$

where,

$|Z(\omega_{pk})| = \sqrt{B(\omega_{pk})^2 + \left( \omega_{pk} \left( m + m_{add}(\omega_{pk}) - \frac{K_{hs}}{\omega_{pk}} \right) \right)^2}$ , is the optimal PTO resistance at a chosen frequency  $\omega_{pk}$ , where  $\omega_{pk}$  is typically the peak of the input wave spectrum.

## References

- [1] López I, Andreu J, Ceballos S, de Alegría IM, Kortabarria I. Review of wave energy technologies and the necessary power-equipment. *Renew Sustain Energy Rev* 2013; 27:413–34.
- [2] Reguero B, Losada I, Méndez F. A global wave power resource and its seasonal, interannual and long-term variability. *Appl Energ* 2015;148:366–80.
- [3] Taveira-Pinto F, Rosa-Santos P, Fazerer-Ferradasa T. Marine renewable energy. *Renew Energy* 2020;150:1160–4.
- [4] Kalogeri C, Galanis G, Spyrou C, Diamantis D, Baladima F, Koukoulia M, Kallos G. Assessing the European offshore wind and wave energy resource for combined exploitation. *Renew Energy* 2017;101:244–64.
- [5] Fusco F, Nolan G, Ringwood JV. Variability reduction through optimal combination of wind/wave resources—An Irish case study. *Energy* 2010;35(1): 314–25.
- [6] Reikard G, Robertson B, Bidlot J-R. Combining wave energy with wind and solar: Short-term forecasting. *Renew Energy* 2015;81:442–56.
- [7] Said HA, Ringwood JV. Grid integration aspects of wave energy—Overview and perspectives. *IET Renew Power Gener* 2021;15:3045–64.
- [8] Wu F, Zhang X-P, Ju P, Sterling MJH. Modeling and control of AWS-based wave energy conversion system integrated into power grid. *IEEE Trans Power Syst* 2008; 23(3):1196–204.
- [9] Wu F, Zhang XP, Ju P, Sterling MJH. Optimal control for AWS-based wave energy conversion system. *IEEE Trans Power Syst* 2009;24(4):1747–55.
- [10] Santana AG, Andrade DEM, Jaén A. Control of hydrodynamic parameters of wave energy point absorbers using linear generators and VSC-based power converters connected to the grid. In: *Int. I Conf. Renew. Energies Power Qual. Spain*; 2010.
- [11] Wu F, Ju P, Zhang X-P, Qin C, Peng G-J, Huang H, Fang J. Modeling, control strategy, and power conditioning for direct-drive wave energy conversion to operate with power grid. *Proc IEEE* 2013;101(4):925–41.
- [12] Marei MI, Mokhtar M, El-Sattar AA. MPPT strategy based on speed control for AWS-based wave energy conversion system. *Renew Energy* 2015;83:305–17.
- [13] Sousounis MC, Gan LK, Kiprakis AE, Shek JKH. Direct drive wave energy array with offshore energy storage supplying off-grid residential load. *IET Renew Power Gener* 2017;11(9):1081–8.
- [14] Jafarishadeh S, Farasat M, Mehraeen S. Grid-connected operation of direct-drive wave energy converter by using HVDC line and undersea storage system. In: *2017 IEEE Energy Convers. Congr. Expo. IEEE*; 2017. p. 5565–71.
- [15] Hasanien HM. Transient stability augmentation of a wave energy conversion system using a water cycle algorithm-based multiobjective optimal control strategy. *IEEE Trans Ind Informatics* 2018;15(6):3411–9.
- [16] Rasool S, Islam MR, Muttaqi KM, Sutanto D. An advanced control strategy for a smooth integration of linear generator based wave energy conversion system with distribution power grids. In: *2019 IEEE Ind. Appl. Soc. Annu. Meet. IEEE*; 2019. p. 1–6.



- [17] Lu K-H, Hong C-M, Han Z, Yu L. New Intelligent Control Strategy Hybrid Grey-RCMAC Algorithm for Ocean Wave Power Generation Systems. *Energies* 2020;13(1):241.
- [18] Rasool S, Islam MR, Muttaqi KM, Sutanto D. Coupled Modeling and Advanced Control for Smooth Operation of a Grid-Connected Linear Electric Generator Based Wave-to-Wire System. *IEEE Trans Ind Appl* 2020;56(5):5575–84.
- [19] Rasool S, Muttaqi KM, Sutanto D. Modelling of a wave-to-wire system for a wave farm and its response analysis against power quality and grid codes. *Renew Energy* 2020;162:2041–55.
- [20] R.A. Turkey, H.M. Hasanien, A. Alkuhayli, Dynamic Stability Improvement of AWS-Based Wave Energy Systems Using a Multiobjective Salp Swarm Algorithm-Based Optimal Control Scheme, *IEEE Syst. Journal* [Early Access].
- [21] Parwal A, Fregelius M, Leijon J, Chatziagiannakou M, Svensson O, Strömstedt E, Temiz I, de Oliveira JG, Boström C, Leijon M. Grid integration and a power quality assessment of a wave-energy park. *IET Smart Grid* 2019;2(4):625–34.
- [22] A. Parwal, M. Fregelius, P. Almeida, O. Svensson, I. Temiz, J.G. Oliveira, C. Boström, M. Leijon, A Comparative Analysis of Linear and Nonlinear Control of Wave Energy Converter for a Force Control Application, *Int. Mar. Energy J. 2* (1 (Nov)) (2019) 39–50.
- [23] Hansen RH. Design and control of the powertake-off system for a wave energy converter with multiple absorbers. Department of Energy Technology, Aalborg University; 2013.
- [24] Sjolte J, Sandvik CM, Tedeschi E, Molinas M. Exploring the potential for increased production from the wave energy converter lifesaver by reactive control. *Energies* 2013;6(8):3706–33.
- [25] de la Villa Jaén A, Santana AG, et al. Considering linear generator copper losses on model predictive control for a point absorber wave energy converter. *Energy Convers Manag* 2014;78:173–83.
- [26] Kelly JF, Wright WM, Sheng W, O'Sullivan K. Implementation and verification of a wave-to-wire model of an oscillating water column with impulse turbine. *IEEE Trans Sustainable Energy* 2015;7(2):546–53.
- [27] Penalba M, Ringwood JV. A review of wave-to-wire models for wave energy converters. *Energies* 2016;9(7):506.
- [28] O'Sullivan ACM, Lightbody G. Co-design of a wave energy converter using constrained predictive control. *Renew Energy* 2017;102:142–56.
- [29] Mendes R, Calado MDR, Mariano S. Maximum power point tracking for a point absorber device with a tubular linear switched reluctance generator. *Energies* 2018;11(9):2192.
- [30] Sousounis MC, Shek J. Wave-to-wire power maximization control for all-electric wave energy converters with non-ideal power take-off. *Energies* 2019;12(15): 2948.
- [31] Penalba M, Ringwood JV. A high-fidelity wave-to-wire model for wave energy converters. *Renewable energy* 2019;134:367–78.
- [32] Huang W, Yang J. A novel piecewise velocity control method using passivity-based controller for wave energy conversion. *IEEE Access* 2020;8:59029–43.
- [33] Karayaka HB, Yu Y-H, Muljadi E. Investigations into balancing peak-to-average power ratio and mean power extraction for a two-body point-absorber wave energy converter. *Energies* 2021;14(12):3489.
- [34] Tedeschi E, Carraro M, Molinas M, Mattavelli P. Effect of control strategies and power take-off efficiency on the power capture from sea waves. *IEEE Trans Energy Conversion* 2011;26(4):1088–98.
- [35] Wang Z, Carrievau R, Ting DS-K, Xiong W, Wang Z. A review of marine renewable energy storage. *Int J Energy Res* 2019;43(12):6108–50.
- [36] W.W. Weaver, D.G. Wilson, A. Hagmuller, M. Ginsburg, G. Bacelli, R.D. Robinett, R. Coe, Others, Super Capacitor Energy Storage System Design for Wave Energy Converter Demonstration, in: 2020 Int. Symp. Power Electron. Electr. Drives, Autom. Motion, IEEE, 2020, pp. 564–570.
- [37] Rojas-Delgado B, Alonso M, Amaris H, de Santiago J. Wave power output smoothing through the use of a high-speed kinetic buffer. *Energies* 2019;12(11): 2196.
- [38] Nie Z, Xiao X, Hiralal P, Huang X, McMahon R, Zhang M, Yuan W. Designing and testing composite energy storage systems for regulating the outputs of linear wave energy converters. *Energies* 2017;10(1):114.
- [39] Forestieri JN, Farasat M. Integrative sizing/real-time energy management of a hybrid supercapacitor/undersea energy storage system for grid integration of wave energy conversion systems, *IEEE. J Emerg Sel Top Power Electron* 2019;8(4): 3798–810.
- [40] Parwal A, Fregelius M, Temiz I, Götteman M, de Oliveira JG, Boström C, Leijon M. Energy management for a grid-connected wave energy park through a hybrid energy storage system. *Appl Energy* 2018;231:399–411.
- [41] García-Violini D, Peña-Sánchez Y, Faedo N, Ringwood JV. An energy-maximising linear time invariant controller (LiTe-Con) for wave energy devices. *IEEE Trans Sustain Energy* 2020;11(4):2713–21.
- [42] W. Cummins, The impulse response function and ship motions. DTIC Document, in: *Proceeding Symp. Sh. Theory Inst. für Schiffbau der Univ. Hambg.*, 1962, pp. 25–27.
- [43] Faedo N, Peña-Sánchez Y, Ringwood JV. Finite-order hydrodynamic model determination for wave energy applications using moment-matching. *Ocean Eng* 2018;163:251–63.
- [44] Y. Peña-Sánchez, N. Faedo, M. Penalba, G. Giorgi, A. Mériçaud, C. Windt, D. García Violini, L. Wang, J.V. Ringwood, Finite-Order hydrodynamic Approximation by Moment-Matching (FOAMM) toolbox for wave energy applications, in: 13th Eur. Wave Tidal Energy Conf. EWTEC, Naples, Italy, 2019.
- [45] Polinder H, Damen MEC, Gardner F. Design, modelling and test results of the AWS PM linear generator. *Eur Trans Electr Power* 2005;15(3):245–56.
- [46] Park RH. Two-reaction theory of synchronous machines generalized method of analysis-part I. *Trans Am Inst Electr Eng* 1929;48(3):716–27.
- [47] Mohan N. *Advanced electric drives: analysis, control, and modeling using MATLAB/Simulink*. John Wiley & sons; 2014.
- [48] Krishna R, Svensson O, Rahm M, Kottayil SK, Waters R, Leijon M. Analysis of linear wave power generator model with real sea experimental results. *IET Renew power Gener* 2013;7(5):574–81.
- [49] El Magri A, Giri F, Besancon G, El Fadili A, Dugard L, Chaoui FZ. Sensorless adaptive output feedback control of wind energy systems with PMS generators. *Control Eng Pract* 2013;21(4):530–43.
- [50] Xu Z, Zhang D, Wang F, Boroyevich D. A unified control for the combined permanent magnet generator and active rectifier system. *IEEE Trans Power Electron* 2014;29(10):5644–56.
- [51] Erickson RW, Maksimovic D. *Fundamentals of power electronics*. Springer Science & Business Media; 2007.
- [52] Hassan M, Paracha ZJ, Armghan H, Ali N, Said HA, Farooq U, Afzal A, Hassan MAS. Lyapunov based adaptive controller for power converters used in hybrid energy storage systems. *Sustainable Energy Technol Assess* 2020;42:100853.
- [53] H. Kanaan, K. Al-Haddad, A comparison between three modeling approaches for computer implementation of high-fixed-switching-frequency power converters operating in a continuous mode, in: *IEEE CCECE2002. Canadian Conference on Electrical and Computer Engineering. Conference Proceedings (Cat. No.02CH37373)*, Vol. 1, 2002, pp. 274–279 vol. 1.
- [54] Sanders SR, Noworolski JM, Liu XZ, Verghese GC. Generalized averaging method for power conversion circuits. *IEEE Trans Power Electron* 1991;6(2):251–9.
- [55] Szczesniak P. A Comparison Between Two Average Modelling Techniques of AC-AC Power Converters. *Int J Power Electron Drive Syst* 2015;6(1):32.
- [56] EirGrid, *Grid Code, Version 6.0*, Tech. rep., EirGrid (2015).
- [57] Salter SH, Taylor J, Caldwell N. Power conversion mechanisms for wave energy. *Proc Inst Mech Eng, Part M: J Eng Maritime Environ* 2002;216(1):1–27.
- [58] D. García-Violini, Y. Peña-Sánchez, N. Faedo, C. Windt, F. Ferri, J.V. Ringwood, Experimental Implementation and Validation of a Broadband LTI Energy-Maximizing Control Strategy for the Wavestar Device, *IEEE Trans. Control Syst. Technol.*
- [59] Faedo N, García-Violini D, Peña-Sánchez Y, Ringwood JV. Optimisation-vs. non-optimisation-based energy-maximising control for wave energy converters: A case study. In: 2020 Eur. Control Conf. IEEE; 2020. p. 843–8.
- [60] García-Violini D, Faedo N, Jaramillo-Lopez F, Ringwood JV. Simple controllers for wave energy devices compared. *J Mar Sci Eng* 2020;8(10):793.
- [61] Overschee PV, De Moor B. *Subspace Identification for Linear Systems - Theory Implication Applications*. Springer; 1996.
- [62] Ljung L. *System Identification - Theory for the User*. Prentice Hall; 1999.
- [63] Kabalan M, Singh P, Niebur D. Large signal Lyapunov-based stability studies in microgrids: A review. *IEEE Trans Smart Grid* 2016;8(5):2287–95.
- [64] Dixon WE, Behal A, Dawson DM, Nagarkatti SP. *Nonlinear control of engineering systems: a Lyapunov-based approach*. Springer Science & Business Media; 2013.
- [65] H. El Fadil, F. Giri, Backstepping based control of PWM DC-DC boost power converters, in: 2007 IEEE Int. Symp. Ind. Electron., IEEE, 2007, pp. 395–400.
- [66] Asensio EM, Magallán GA, De Angelo CH, Serra FM. Energy management on battery/ultracapacitor hybrid energy storage system based on adjustable bandwidth filter and sliding-mode control. *J Energy Storage* 2020;30:101569.
- [67] Said HA, Ringwood JV. Intelligent control of a DC microgrid consisting of Wave Energy Converter (WEC) and Hybrid Energy Storage System (HESS). In: 14th European Wave and Tidal Energy Conference (EWTEC). Plymouth; 2021. pp. 1884–1, 1884–9.
- [68] Sanders SR, Verghese GC. Lyapunov-based control for switched power converters. *IEEE Trans Power Electron* 1992;7(1):17–24.
- [69] Golestan S, Guerrero JM, Vasquez JC. Three-phase PLLs: A review of recent advances. *IEEE Trans Power Electron* 2016;32(3):1894–907.
- [70] K.F. Hasselmann, T.P. Barnett, E. Bouws, H. Carlson, D.E. Cartwright, K. Eake, J.A. Euring, A. Gicnapp, D.E. Hasselmann, P. Kruseman, Others, Measurements of wind-wave growth and swell decay during the Joint North Sea Wave Project (JONSWAP)., *Ergaenzungsh. zur Dtsch. Hydrogr. Zeitschrift*, R.A.
- [71] Papoulis A. *Probability, Random Variables and Stochastic Processes*. New York, NY, USA: McGraw-Hill; 1991.
- [72] Giorgi G, Ringwood JV. Analytical representation of nonlinear Froude-Krylov forces for 3-DoF point absorbing wave energy devices. *Ocean Eng* 2018;164: 749–59.
- [73] Fusco F, Ringwood JV. A study of the prediction requirements in real-time control of wave energy converters. *IEEE Trans Sustainable Energy* 2011;3(1):176–84.
- [74] Peña-Sánchez Y, Windt C, Davidson J, Ringwood JV. A critical comparison of excitation force estimators for wave-energy devices. *IEEE Trans Control Syst Technol* 2019;28(6):2263–75.
- [75] Wahyudie A, Saeed O, Jama M, Noura H, Harib K. Maximising power conversion for heaving point absorbers using a reference-based control technique. *IET Renew power Gener* 2017;11(3):271–80.
- [76] Jama M, Mon BF, Wahyudie A, Mekhilef S. Maximum Energy Capturing Approach for Heaving Wave Energy Converters Using an Estimator-Based Finite Control Set Model Predictive Control. *IEEE Access* 2021;9:67648–59.

- [77] Sergiienko NY, Bacelli G, Coe RG, Cazzolato BS. A comparison of efficiency-aware model-predictive control approaches for wave energy devices. *J Ocean Eng Marine Energy* 2021;1–13.
- [78] Li X, Chen C, Li Q, Xu L, Liang C, Ngo K, Parker RG, Zuo L. A compact mechanical power take-off for wave energy converters: Design, analysis, and test verification. *Appl Energy* 2020;278:115459.
- [79] Montoya D, Tedeschi E, Castellini L, Martins T. Passive Model Predictive Control on a Two-Body Self-Referenced Point Absorber Wave Energy Converter. *Energies* 2021;14(6):1731.
- [80] B. Wen, D. Boroyevich, R. Burgos, P. Mattavelli, Z. Shen, Analysis of dq small-signal impedance of grid-tied inverters, *IEEE Trans. Power Electron.* 31 (1) (2015) 675–687.
- [81] X. Zhang, D. Xia, Z. Fu, G. Wang, D. Xu, An improved feedforward control method considering pll dynamics to improve weak grid stability of grid-connected inverters, *IEEE Trans. Ind. Appl.* 54 (5) (2018) 5143–5151.
- [82] I. o. E. a. E.E. IEEE, IEEE Std. 519–1992: Recommended Practices and Requirements for Harmonic Control in PowerSystems, Tech. rep. (1993).
- [83] Paparella F, Ringwood JV. Optimal control of a three-body hinge-barge wave energy device using pseudospectral methods. *IEEE Trans Sustain Energy* 2016;8(1): 200–7.